Article

Molecular Cell

Functional Domains of NEAT1 Architectural lncRNA Induce Paraspeckle Assembly through Phase Separation

Graphical Abstract

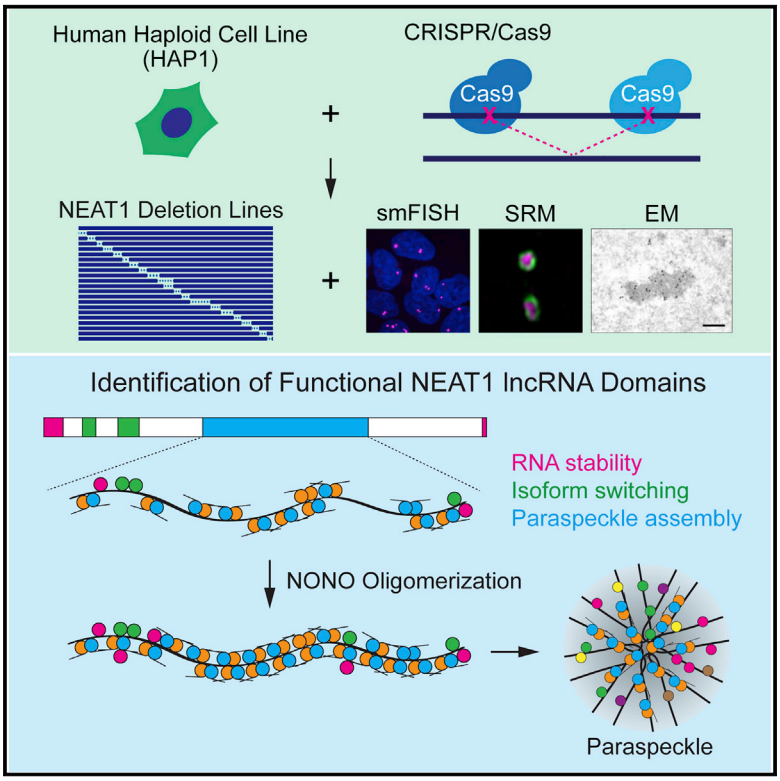

Authors

Tomohiro Yamazaki, Sylvie Souquere, Takeshi Chujo, ..., Shinichi Nakagawa, Gerard Pierron, Tetsuro Hirose

Correspondence

hirose@igm.hokudai.ac.jp

In Brief

The NEAT1 architectural noncoding RNA has a modular domain structure with distinct functions required for paraspeckle formation. Among the functional domains, the middle domain is composed of three distinct, functionally redundant, subdomains that recruit NONO dimers to initiate assembly of the phase-separated paraspeckle structure.

Highlights

- NEAT1 possesses a modular domain structure with distinct functions to build paraspeckles
- The NEAT1_2 middle domain is necessary and sufficient for paraspeckle assembly
- NEAT1_2 middle subdomains recruit NONO dimers that initiate paraspeckle assembly
- NEAT1_2 subdomains can induce aggregation of NONO dimers *in vitro*

Yamazaki et al., 2018, Molecular Cell *70*, 1038–1053
June 21, 2018 © 2018 Elsevier Inc.
https://doi.org/10.1016/j.molcel.2018.05.019

CellPress

CellPress

Molecular Cell
Article

Functional Domains of NEAT1 Architectural lncRNA Induce Paraspeckle Assembly through Phase Separation

Tomohiro Yamazaki,[1] Sylvie Souquere,[2] Takeshi Chujo,[1] Simon Kobelke,[3] Yee Seng Chong,[4] Archa H. Fox,[3] Charles S. Bond,[4] Shinichi Nakagawa,[5] Gerard Pierron,[2] and Tetsuro Hirose[1,6,*]

[1]Institute for Genetic Medicine, Hokkaido University, Sapporo 060-0815, Japan
[2]Centre National de la Recherche Scientifique, UMR-8122, Institut Gustave Roussy, Villejuif 94805, France
[3]School of Human Sciences, University of Western Australia, Crawley, WA 6009, Australia
[4]School of Molecular Sciences, University of Western Australia, Crawley, WA 6009, Australia
[5]Faculty of Pharmaceutical Sciences, Hokkaido University, Sapporo 060-0812, Japan
[6]Lead Contact
*Correspondence: hirose@igm.hokudai.ac.jp
https://doi.org/10.1016/j.molcel.2018.05.019

SUMMARY

A class of long noncoding RNAs (lncRNAs) has architectural functions in nuclear body construction; however, specific RNA domains dictating their architectural functions remain uninvestigated. Here, we identified the domains of the architectural NEAT1 lncRNA that construct paraspeckles. Systematic deletion of NEAT1 portions using CRISPR/Cas9 in haploid cells revealed modular domains of NEAT1 important for RNA stability, isoform switching, and paraspeckle assembly. The middle domain, containing functionally redundant subdomains, was responsible for paraspeckle assembly. Artificial tethering of the NONO protein to a NEAT1_2 mutant lacking the functional subdomains rescued paraspeckle assembly, and this required the NOPS dimerization domain of NONO. Paraspeckles exhibit phase-separated properties including susceptibility to 1,6-hexanediol treatment. RNA fragments of the NEAT1_2 subdomains preferentially bound NONO/SFPQ, leading to phase-separated aggregates *in vitro*. Thus, we demonstrate that the enrichment of NONO dimers on the redundant NEAT1_2 subdomains initiates construction of phase-separated paraspeckles, providing mechanistic insights into lncRNA-based nuclear body formation.

INTRODUCTION

Long noncoding RNAs (lncRNAs) have recently been recognized as fundamental regulators of gene expression, but their mechanisms of action remain largely unknown. Unlike protein-coding mRNAs, lncRNAs per se form complex machineries with multiple RNA-binding proteins (RBPs) (Engreitz et al., 2016; Quinn and Chang, 2016). However, specific sequences or structural elements embedded in lncRNA sequences required for building the functional machinery have been poorly investigated. A limited number of lncRNAs are known to have modular domain compositions; for example, XIST requires the A-repeat domain comprising nine repetitive stem-loop structures for gene silencing on the inactivated X chromosome in mammalian cells (Wutz et al., 2002). SPEN interacts with the A-repeat domain and is required for gene silencing (Chu et al., 2015).

Among tens of thousands of human lncRNAs, several lncRNAs function as the structural scaffolds of membraneless subnuclear structures or nuclear bodies (NBs) (Chujo et al., 2016). NBs are located in the inter-chromatin spaces in the highly organized nucleus and consist of specific factors that function in various nuclear processes (Banani et al., 2017). Some NBs exhibit liquid-like properties, and RBP components of NBs containing the prion-like domain (PLD), low complexity domains, or intrinsically disordered regions induce liquid-liquid phase separation (LLPS) to form liquid droplets. This raises the intriguing possibility that LLPS is the driving force for NB formation (Banani et al., 2017; Staněk and Fox, 2017). RNA accelerates LLPS *in vitro* by sequestration of PLD-containing RBPs and/or alteration of their conformation (Shin and Brangwynne, 2017). Thus, RNA sequences that specifically interact with PLD-containing RBPs can induce LLPS.

Several NBs contain specific lncRNA species that play architectural roles in their formation (Chujo et al., 2016). For example, NEAT1 serves as an essential architectural component of paraspeckle NBs (Clemson et al., 2009; Sasaki et al., 2009; Sunwoo et al., 2009). Paraspeckles were initially defined as the foci found in close proximity to nuclear speckles and are enriched with characteristic DBHS (*Drosophila* Behavior Human Splicing) RBPs including NONO, SFPQ, and PSPC1 (Fox et al., 2002; Visa et al., 1993). NEAT1 is transcribed from a specific locus in human chromosome 11 by RNA polymerase II (RNAPII) to produce two distinct isoforms, NEAT1_1 (3.7 kb) or NEAT1_2 (22.7 kb), as a consequence of alternative 3′ end processing (Naganuma et al., 2012). NEAT1_2 but not NEAT1_1 is indispensable for paraspeckle formation (Naganuma et al., 2012). NEAT1_1 is canonically polyadenylated, whereas NEAT1_2 lacks a poly(A) tail and instead contains a triple helix (TH)

structure at its 3′ terminus (Sunwoo et al., 2009; Wilusz et al., 2012). Electron microscopic (EM) and super-resolution microscopic (SRM) analyses revealed that the paraspeckle is a highly ordered, spheroidal structure in which the 5′ terminus of NEAT1 and 3′ terminus of NEAT1_2 are located in the outer shell, whereas the middle region of NEAT1_2 is located in the inner core (Souquere et al., 2010; West et al., 2016). Paraspeckle formation is tightly coupled with ongoing RNAPII transcription of NEAT1_2 and with the binding of multiple paraspeckle proteins (PSPs) to NEAT1 (Mao et al., 2011). More than 60 PSPs, most of which are RBPs, have been identified (Yamazaki and Hirose, 2015). Functional categorization of PSPs by extensive RNAi analysis revealed seven category 1 proteins essential for formation of a paraspeckle with ~50 NEAT1_2 molecules (Chujo et al., 2017; Naganuma et al., 2012). Among the seven category 1 proteins, six possess characteristic PLDs (Yamazaki and Hirose, 2015). The PLDs of FUS and RBM14 form hydrogels *in vitro* and are required for paraspeckle formation *in vivo* (Hennig et al., 2015). In addition, SWI/SNF chromatin remodeling complexes play an essential role in paraspeckle assembly without requiring their ATP-dependent remodeling activity (Kawaguchi et al., 2015). Transcription of NEAT1 is upregulated by various conditions, resulting in an increase in the size and number of paraspeckles, which can sequestrate specific RBPs and/or RNAs away from the nucleoplasm to control gene expression (Chen and Carmichael, 2009; Hirose et al., 2014). Physiologically, NEAT1 is required for the development of specific tissues such as the corpus luteum in mice and is involved in the progression of various cancers (Adriaens et al., 2016; Nakagawa et al., 2014).

Despite growing knowledge of the roles of PSPs during paraspeckle formation, it is not known what parts of NEAT1_2 are responsible for its architectural roles. By carrying out CRISPR/Cas9-mediated systematic deletions of portions of NEAT1_2 in the human haploid cell line, we revealed the modular domain structure of NEAT1_2 with three functionally distinct domains important for (1) stabilization of NEAT1_2, (2) NEAT1 isoform switching, and (3) paraspeckle assembly. The middle domain, which is necessary and sufficient for paraspeckle assembly, contains three functional subdomains. Artificial tethering of each of three category 1 proteins to a functionally defective NEAT1_2 mutant rescued paraspeckle formation, and the rescue activity required the NOPS dimerization domain of NONO. Paraspeckles were disintegrated by treatment with 1,6-hexanediol (1,6-HD) in a similar manner to other phase-separated NBs. The RNA fragments of the NEAT1_2 subdomain preferentially bound NONO and SFPQ and induced higher-order assembly *in vitro*. In summary, we argue that the identified NEAT1_2 subdomains recruit the NONO dimer to initiate oligomerization with other PSPs, promoting formation of the phase-separated paraspeckle structure. Our findings provide fundamental insights into the formation of NBs built on architectural lncRNAs (arcRNAs).

RESULTS

The 3′ Terminal TH Structure Stabilizes NEAT1_2 lncRNA *In Vivo*

To investigate the functional domains of NEAT1 lncRNA, we set up an experimental system using CRISPR/Cas9 genome editing in the human haploid cell line HAP1. We deleted various portions of NEAT1 by expressing CRISPR/Cas9 proteins and one or two single-guide RNAs (sgRNAs) (Figure 1A). We first targeted the TH structure of NEAT1_2 to validate our system. We established two HAP1 clones carrying deletions of a part of the conserved stem loop and U-rich motif 2 in the TH (ΔTH#1 and #2 in Figure 1B). Single-molecule FISH (smFISH) was employed to observe the paraspeckles in these clones. Our smFISH specifically detected NEAT1 because no smFISH signals were detected in NEAT1 knockout (KO) cells (ΔNEAT1) (Figures S1A–S1D). In the ΔTH clones, paraspeckles were almost undetectable by smFISH and conventional RNA-FISH (Figures 1C, 1D, and S1E–S1G). RT-qPCR and RNase protection assay (RPA) revealed considerably lower levels of NEAT1_2, but not NEAT1_1, in the ΔTH clones than in the wild-type (WT) (Figures 1E, 1F, and S1H). Furthermore, NEAT1_2 in ΔTH cells was much more unstable than in WT cells (Figure 1G). Thus, TH stabilizes NEAT1_2 *in vivo*.

NEAT1 lncRNA Domains Required for Expression, Isoform Switching, and Paraspeckle Formation

We next investigated the RNA domains of NEAT1 required for its expression and for paraspeckle formation. To explore the entire region of NEAT1, we established HAP1 clones lacking portions of NEAT1 (0.6–1.9 kb) as shown in Figure 2A and examined two independent clones for each mutant to validate their phenotypes by smFISH and RT-qPCR of NEAT1_1 and NEAT1_2 (Figures S2A and S2B). Overall, the expression levels of NEAT1_2 were positively correlated with the presence of paraspeckles (Figures S2A–S2C). Among these deletion clones, paraspeckles did not form in the deletion lines Δ0–1k, Δ2.1–2.8k, and Δ4–5.1k (k for kb) (Figures 2B, 2C, and S2A–S2C).

In the Δ0–1k clones, levels of NEAT1_1 and NEAT1_2 were markedly lower than in the WT, as determined by RT-qPCR and RPA (Figures 2D and 2F). This reduction was partly caused by destabilization of NEAT1_1 and NEAT1_2 (Figure 2G). In Δ0–1k cells, the marked disappearance of paraspeckles is likely to be a consequence of the strong reduction in NEAT1_2, suggesting that this 5′ terminal region contains specific elements for NEAT1 expression, which is further supported by experiments to narrow down the functional domain within the 0- to 1-kb region (Figures S2D–S2H).

In the Δ2.1–2.8k and Δ4–5.1k clones, the expression levels of NEAT1_2 were significantly lower than in the WT, whereas NEAT1_1 levels were 2- to 2.5-fold higher (Figures 2E and S2C–S2H). As these regions were located close to the polyadenylation signal (PAS) of NEAT1_1, we supposed that these domains are involved in the alternative 3′ end processing, facilitating NEAT1_2 synthesis by inhibiting the usage of NEAT1_1 PAS. To test this possibility, we established HAP1 cell lines carrying deletions of PAS alone (ΔPAS), both ΔPAS and Δ2.1–2.8k (Δ2.1–2.8k/ΔPAS), and both ΔPAS and Δ4–5.1k (Δ4–5.1k/ΔPAS) (Figure 2A). Deletion of PAS alone caused a strong reduction in NEAT1_1 and slight upregulation of NEAT1_2, not affecting the appearance of paraspeckles (Figures 2H–2J). Unlike Δ2.1–2.8k or Δ4–5.1k clones, Δ2.1–2.8k/ΔPAS and Δ4–5.1k/ΔPAS clones showed comparable expression of NEAT1_2 to the WT, and paraspeckles were clearly observed

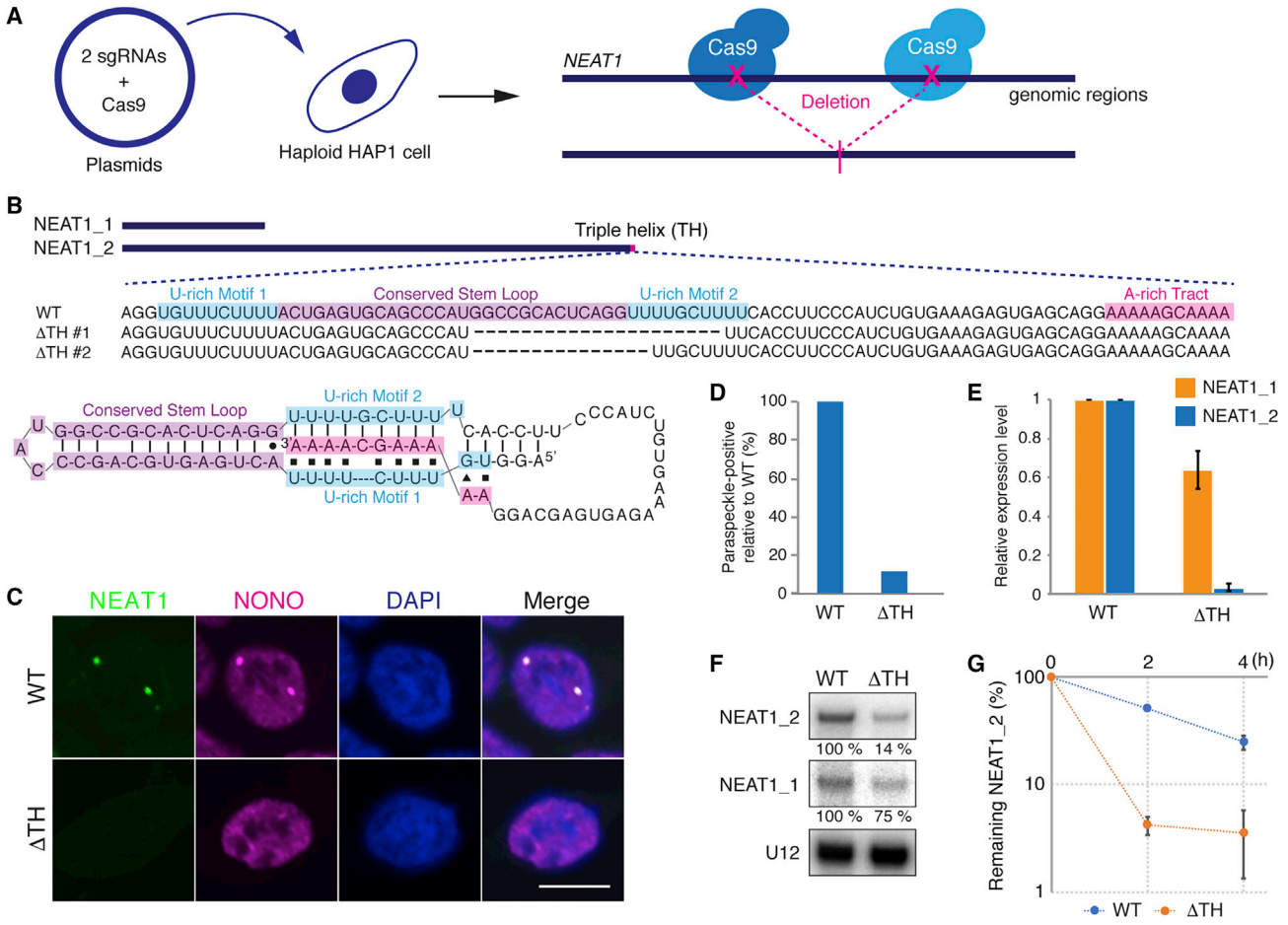

Figure 1. The TH Structure Stabilizes NEAT1_2 lncRNA *In Vivo*

(A) The experimental strategy of CRISPR/Cas9-mediated partial deletion of the NEAT1 gene in human haploid HAP1 cells. The plasmid harboring two sgRNAs and Cas9 was transfected into HAP1 cells followed by clonal selection of mutant cells.

(B) The sequence and structure of the TH at the 3′ terminus of wild-type human NEAT1_2 (WT) and two deletion mutants (ΔTH#1 and ΔTH#2). Single dash: Watson-Crick base pair, black square: Hoogsteen interaction, black circle: noncanonical base pair, black triangle: A-minor interaction.

(C) Paraspeckles in ΔTH cells were detected by FISH of NEAT1 (green) and immunofluorescence (IF) of NONO (magenta), and the nuclei were stained with DAPI. Scale bar, 10 μm.

(D) Quantitation of paraspeckle-positive cells in (C) (WT: 100%).

(E) Quantitation of NEAT1 isoforms by RT-qPCR in WT and ΔTH cells. Data are represented as mean ± SD (n = 3).

(F) Assessment of NEAT1 isoform levels by RPA in WT and ΔTH cells. The quantitated band intensities (WT: 100%) are shown below each panel. U12 is a loading control.

(G) Stability of NEAT1_2 was quantitated by RT-qPCR of the pulse-labeled RNA with 5-bromouridine (5-BrU). Data are represented as mean ± SD (n = 3).

(Figures 2H–2J). Therefore, NEAT1 2.1–2.8 kb and 4–5.1 kb domains suppress NEAT1_1 PAS-dependent polyadenylation.

The Middle Domain of NEAT1_2 Is Required for Ordered Paraspeckle Assembly

Several lncRNAs like XIST reportedly possess repeated sequence stretches that have important functional roles (Chu et al., 2015; Wutz et al., 2002). Comparison of the NEAT1_2 sequence with itself using the BLAST algorithm revealed the presence of several repetitive sequences with varying length and similarity among three mammalian species (Figure S3A). Some of the repetitive sequences in human NEAT1_2 overlapped with annotated LINE and SINE elements (Figure S3B). To investigate the importance of these repetitive sequences, we deleted the middle portion (8–16.6 kb) of NEAT1_2 (Δmiddle in Figure 3A), which contains multiple long repetitive sequences and is localized in the core of the paraspeckle. In the Δmiddle cells, we observed tiny dispersed foci (Figures 3B and S3C). A similar phenotype was observed in another distinct Δmiddle cell line (Δmiddle#2), which was established with another set of sgRNAs, under both MG132-untreated and -treated conditions (Figure S3C). We determined paraspeckle sizes by measuring the area and sum signal intensity of each focus in cells with or without MG132 treatment (Figures 3C and S3D). MG132 induces NEAT1 transcription to enlarge paraspeckles (Hirose et al., 2014). The size and smFISH signal intensity of paraspeckles in

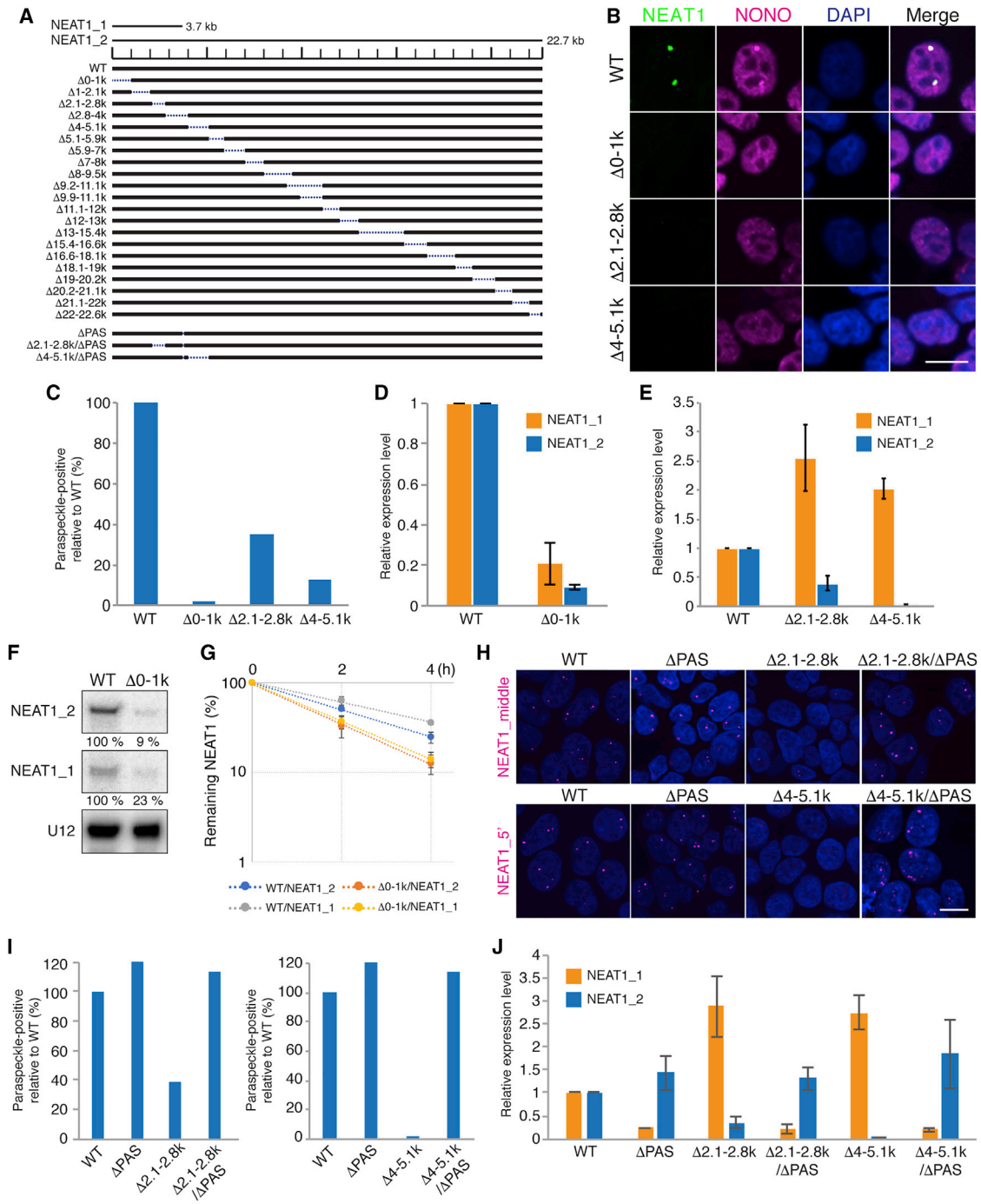

Figure 2. Identification of NEAT1 Domains Required for Expression, Isoform Switching, and Paraspeckle Formation

(A) The scanning deletion mutants of human NEAT1_2. The NEAT1 transcripts are shown above with a scale. The blue dashed lines represent the deleted regions.

(B) NEAT1 FISH (green) and NONO IF (magenta) with DAPI staining (blue) in NEAT1 deletion mutants. Scale bar, 10 μm.

(C) Quantitation of paraspeckle-positive cells in the cell lines in (B) (WT: 100%).

(D and E) RT-qPCR of NEAT1 isoforms in WT and Δ0–1k cells (D) or Δ2.1–2.8k and Δ4–5.1k cells (E). Data are represented as mean ± SD (n = 3).

(F) RPA to detect NEAT1 isoforms in WT and Δ0–1k cells. The quantitated band intensities (WT: 100%) are shown below each panel. U12 is a loading control.

(G) Quantitation of the RNA stability of NEAT1_1 and NEAT1_2 in WT and the mutant cell line by RT-qPCR of the pulse-labeled RNA with 5-BrU. Data are represented as mean ± SD (n = 3).

(legend continued on next page)

Δmiddle were significantly lower than in the WT (Figures 3C and S3D), although the NEAT1_2 expression levels were comparable to those in the WT (Figure S3E). Therefore, the middle region is required for paraspeckle assembly rather than NEAT1_2 expression. Similarly, dispersed foci were observed in FUS KO cells, which are defective in paraspeckle assembly without affecting NEAT1_2 levels (Chujo et al., 2017; West et al., 2016) (Figures 3C and S3C–S3E). Another large deletion of a different region of NEAT1_2 (Δ13–20.2k) did not significantly affect the integrity of paraspeckles (Figures 3B, 3C, S3C, and S3D), excluding the possibility that Δmiddle NEAT1 was too short to form paraspeckles. Thus, the middle domain is specifically required for paraspeckle integrity.

To clarify the ultra-structures of the paraspeckles in Δmiddle cells, we used EM. Previous EM analyses showed that paraspeckles are highly ordered (Souquere et al., 2010). As reported, the probes against the NEAT1 5′ region detected the surface of paraspeckles in WT and Δ13–20.2k cells. By contrast, in Δmiddle cells, the same 5′ probes randomly detected both the surface and interior of the paraspeckles (Figure 3D, upper panels), showing that the paraspeckle structure became disordered in Δmiddle cells. We measured the size of paraspeckles characterized by the electron dense NONO-positive oval foci in the WT, Δmiddle, and Δ13–20.2k (Figure 3D, lower panels). Diameters of the short (Sx) and long (Lx) axes of paraspeckles in Δmiddle cells and not Δ13–20.2k cells were significantly smaller than in the WT, thereby shrinking the surface area (Figures 3E, S3F, and S3G).

Next, we examined *de novo* formation of paraspeckles in WT, Δmiddle, and Δ13–20.2k cells using 5,6-dichloro-1-β-D-ribofuranosylbenzimidazole (DRB), a reversible inhibitor of RNAPII. During DRB treatment, NEAT1 levels decreased in the three cell lines and increased upon release from DRB (Figure S3H). Accordingly, DRB treatment disintegrated paraspeckles, and upon washing out DRB, paraspeckles formed *de novo*. SRM analyses revealed that paraspeckles formed *de novo* in the WT and Δ13–20.2k had an ordered core-shell structure, whereas the structure was disordered in Δmiddle (Figure 3F). Therefore, the assembly step of paraspeckles was defective in Δmiddle. Consistent with the importance of the middle domain, the essential PSPs including NONO, SFPQ, and FUS were mainly localized in the core of WT paraspeckles where the NEAT1_2 middle domain is located (Figures 3F and S3I).

The Middle Domain of NEAT1_2 Is Sufficient for Formation of the Ordered Paraspeckle Structure with a Phase Separated Feature

Based on the functional domains of NEAT1 identified above, we next explored the minimal regions of NEAT1_2 required for paraspeckle formation. We established HAP1 clones that contained only the expression domains (5′ terminal region and the 3′ TH) and the middle domain (8–16.6 kb) required for paraspeckle assembly (Figure 4A). SRM showed that this mutant, termed mini-NEAT1, could form an ordered paraspeckle structure (Figure 4B). EM observation of the mini-NEAT1 paraspeckles also supported their ordered structure with the interior localization of NONO, patchy localization of BRG1, surface localization of NEAT1–5′, and interior localization of the NEAT1_2 middle region, all of which are consistent with the patterns in the WT (Kawaguchi et al., 2015; Souquere et al., 2010) (Figures 4F and 4G). Despite the ordered structure, the mini-NEAT1 paraspeckles were smaller with shorter Lx and Sx than those in WT cells (Figure 4H). Mini-NEAT1 was expressed at a comparable level to WT NEAT1 (Figure 4D). Unlike WT paraspeckles in which the 3′ end of NEAT1_2 is located in the shell, the 3′ end of mini-NEAT1 was located in the core (Figures 4A–4C and 4E). These data suggest that the shortened length of mini-NEAT1 (9.7 kb) and its configuration reflect the decreased size of paraspeckles. An essential PSP, SFPQ was less efficiently recruited to the mini-NEAT1 paraspeckles than to WT paraspeckles, but other essential PSPs were recruited to these foci (Figure S4A).

Paraspeckles, which have a core-shell spheroidal structure, have been reported to be dynamic NBs, into which and from which a proportion of PSPs (∼60%–75%) dynamically migrate in and out (Mao et al., 2011). Additionally, PLDs of PSPs are required for paraspeckle formation *in vivo*, and recombinant PLD of PSPs can induce phase separation *in vitro* (Hennig et al., 2015). These results raised the possibility that paraspeckles are phase-separated structures. To investigate this, we employed 1,6-HD, which can disrupt several phase-separated subcellular structures *in vivo* by disrupting their multivalent hydrophobic interactions (Kroschwald et al., 2015; Lin et al., 2016; Shin and Brangwynne, 2017). After treatment with 6%–10% 1,6-HD, the intact paraspeckles, in which NEAT1 and NONO should be co-localized, disappeared in both HAP1 WT and mini-NEAT1 cells (Figures 4I and 4J), suggesting that the paraspeckles are sensitive to 1,6-HD and thus are likely phase-separated in these cells. In the same experimental conditions, Cajal bodies, which were labeled with COIL and are known to be phase-separated (Lin et al., 2016), were readily disintegrated (Figure S4F). On the other hand, nuclear speckles labeled with SRSF2 were not significantly affected (Figure S4F), showing that our 1,6-HD condition was mild enough not to disrupt all subcellular structures. 2,5-hexanediol (2,5-HD) is an aliphatic alcohol like 1,6-HD but does not affect phase-separated cellular structures (Lin et al., 2016). As expected, even in the presence of 10% 2,5-HD, the paraspeckles were clearly visible (Figure S4G). Next, we examined the paraspeckle substructure by SRM in the presence of 1,6-HD or 2,5-HD. Disrupted structures were observed in the 1,6-HD-treated condition, while ordered paraspeckle structures were clearly observed in the 2,5-HD-treated condition (Figure 4K). Co-immunoprecipitation (coIP) revealed that interactions of NONO with RBM14 and FUS were markedly weakened by 1,6-HD washing buffer (Figure 4L), suggesting that these interactions are part of the effector sites for 1,6-HD. Together with previous reports, these data suggest that the

(H) Detection of paraspeckles in the WT and five mutant cell lines by smFISH with a NEAT1 middle probe (upper panels) and NEAT1_5′ probe (lower panels) to detect NEAT1_2 and both NEAT1_1 and NEAT1_2, respectively. Scale bar, 10 μm.
(I) Quantitation of paraspeckle-positive cells in the mutants used in (H) (WT: 100%).
(J) RT-qPCR of the NEAT1 isoforms in the mutant cells used in (H) (WT = 1). Data are represented as mean ± SD (n = 3).

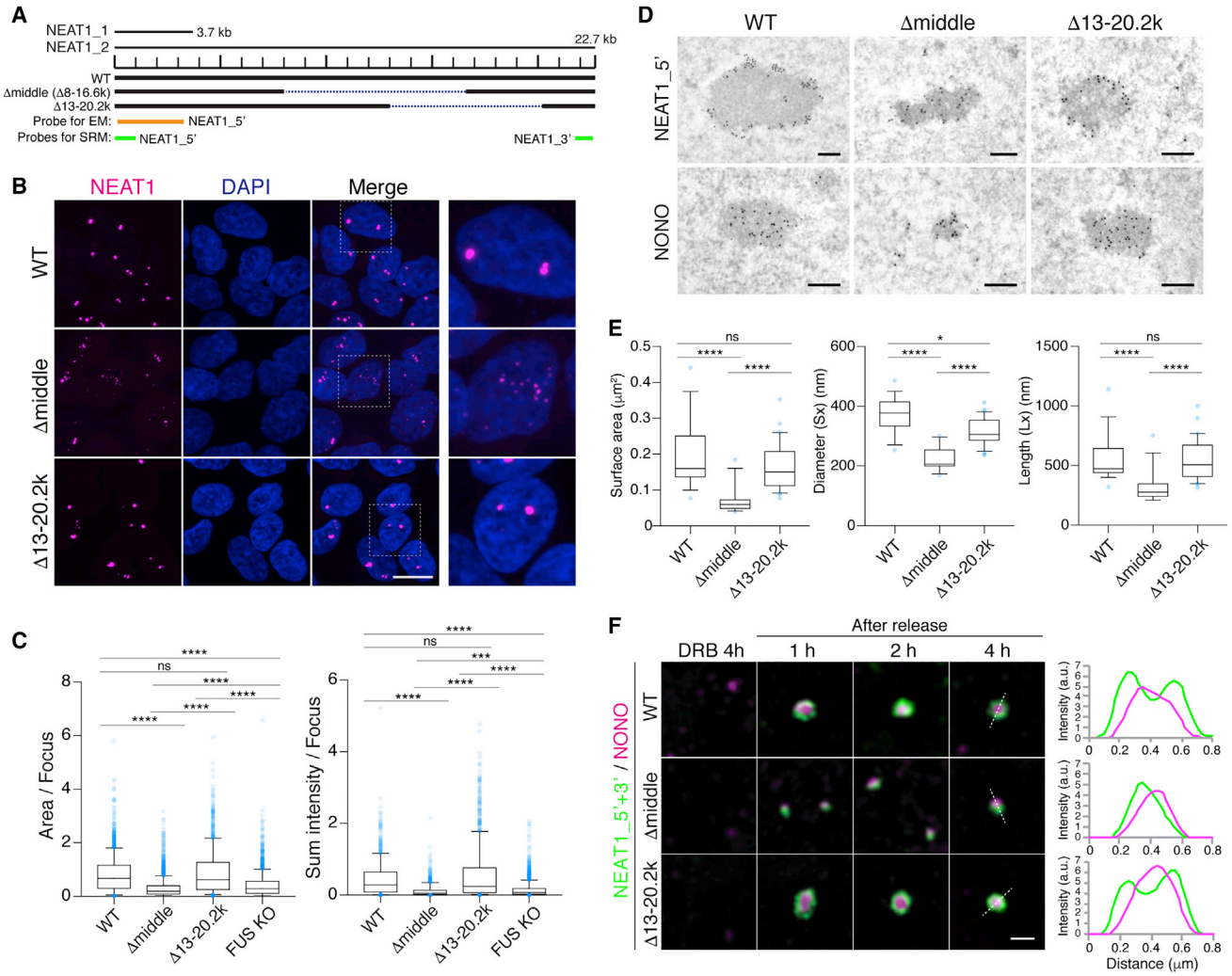

Figure 3. The Middle Domain of NEAT1_2 Is Required for Ordered Paraspeckle Assembly

(A) The schematics of the WT and the mutants with the larger deletions of two middle regions (Δmiddle and Δ13–20.2k) are shown as in Figure 2A. The positions of the NEAT1_5′ antisense probes used for EM, and NEAT1_5′ and NEAT1_3′ antisense probes for SRM, are shown below with orange and green lines, respectively.

(B) Detection of paraspeckles in the three cell lines in (A). Paraspeckles are detected by RNA-FISH with the NEAT1 5′ smFISH probe after treatment with 5 μM MG132 for 6 hr. Magnified images of the areas indicated by the dashed boxes are shown on the right. Scale bar, 10 μm.

(C) Quantitative analyses of sizes of the NEAT1 foci in the cells treated with 5 μM MG132 for 6 hr (****$p < 0.0001$, ***$p < 0.001$; ns, not significant)

(D) EM observation of the paraspeckles in the three cell lines in (A). The localization of the 5′ terminus of NEAT1 (upper panels) or NONO (lower panels) was detected with a NEAT1–5′ probe or NONO antibodies labeled with gold particles, respectively. To enlarge the paraspeckles, the HAP1 cells were treated with 5 μM MG132 for 17 hr (upper panels). Scale bars, 200 nm.

(E) Quantitation of the paraspeckle sizes observed by EM after treatment with 5 μM MG132 for 4 hr (****$p < 0.0001$, *$p < 0.05$; ns, not significant.)

(F) Observation of the *de novo* synthesized paraspeckles in the three cell lines in (A) by SRM. The cells were treated with DRB (50 μM) for 4 hr and then released for 1, 2, and 4 hr to observe paraspeckles by RNA-FISH using a mixture of NEAT1_5′ and NEAT1_3′ probes (green) and IF of NONO (magenta). Line profiles of the paraspeckles at 4 hr after DRB release are shown (right). Scale bar, 500 nm.

paraspeckles in WT and mini-NEAT1 cells are phase-separated *in vivo*.

NEAT1_2 Middle Domain Contains Multiple Redundant Subdomains for Ordered Paraspeckle Assembly

To identify which part of the NEAT1_2 middle domain is required for paraspeckle assembly, we established additional deletion mutants (Figure 5A, upper). NEAT1 expression levels in these clones were comparable (Figures S5A and S5B), and all new deletion mutants showed significant defects in paraspeckle formation, although these defects were milder than defects in Δmiddle cells (Figures 5B, 5C, S5C, and S5D). Using SRM, we quantified the ratio of ordered and disordered paraspeckles. Consistent with the smFISH results in Figures 5B and 5C, all the deletion mutants showed defects in formation of ordered paraspeckle structures (Figures 5D and 5E). In particular, Δ8–15.4k mutants showed a strong defect, and the remaining mutants (Δ8–13k, Δ8–11.1k, and Δ11.1–16.6k) exhibited milder

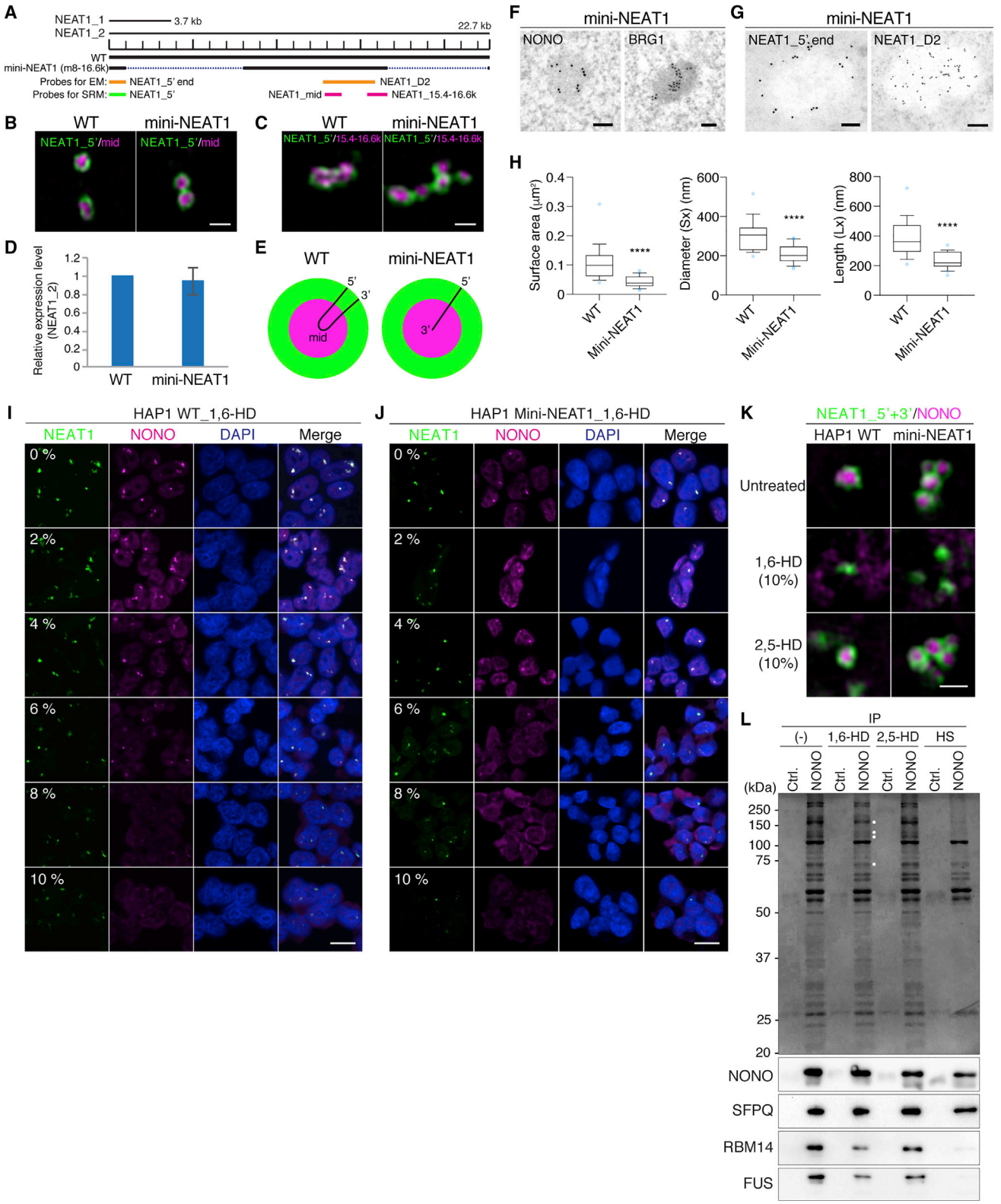

Figure 4. The Middle Domain of NEAT1_2 Is Sufficient for Formation of the Ordered Paraspeckle Structure

(A) The schematics of the WT and mini-NEAT1 mutant (m8–16.6k) are shown with a scale as in Figure 2A. The positions of the NEAT1_5′ and NEAT1_D2 probes used for EM (orange), and the NEAT1_5′ (green), NEAT1_mid (magenta), and NEAT1_15.4–16.6k (magenta) probes used for SRM, are shown below.

(legend continued on next page)

but significant defects (Figures 5D and 5E). These data suggest that the whole middle domain contributes to paraspeckle assembly.

As an alternative approach to dissect the middle domain of NEAT1_2, deletion mutants were established based on mini-NEAT1 (Figure 5A, lower). NEAT1_2 was detected at comparable levels in all the new mutants (Figure S5E), and SRM showed that the mutants m9.2–16.6k, m9.8–16.6k, m11.1–16.6k, and m12–16.6k (m for mini-NEAT1) could predominantly form ordered structures (Figures 5F and 5G). By contrast, m13–16.6k and m8–15.4k could only form tiny disordered structures (Figures 5F and 5G), suggesting that the 12- to 13-kb and 15.4- to 16.6-kb regions are functional subdomains for paraspeckle assembly. It should be noted that the stepwise deletions from 9.8 to 12 kb gradually decreased the ratio of ordered paraspeckles (Figure 5G), suggesting the presence of redundant subdomains in this region. We thus examined whether the 12- to 13-kb region was solely required for the formation of ordered paraspeckles in the m9.8–16.6k mutant in which ordered paraspeckles were formed. To this end, we established HAP1 clones lacking the 12- to 13-kb region in m9.8–16.6k (Δ12–13k/m9.8–16.6k in Figure 5A, lower). SRM showed the presence of ordered paraspeckles in these cells (Figures 5F and 5G), showing that 9.8- to 12-kb and 12- to 13-kb regions function redundantly in the formation of ordered paraspeckles. These data collectively demonstrate that the middle domain contains multiple redundant subdomains for paraspeckle assembly.

An Essential NEAT1_2 Subdomain Can Be Functionally Replaced by Artificially Tethered Essential PSPs

We next investigated the role of the identified functional subdomains of NEAT1_2 (9.8–12 kb, 12–13 kb, and 15.4–16.6 kb) in paraspeckle assembly. We hypothesized that these subdomains recruit the PSPs essential for paraspeckle assembly. We examined whether tethering of PSPs to a functionally defective NEAT1_2 can rescue paraspeckle assembly. We introduced 6 × MS2-binding sites (6 × MS2BS) at 14 kb of NEAT1_2 in m13–16.6k cells (m13–16.6k/6 × MS2BS) (Figure 6A). We selected four essential PSPs (NONO, SFPQ, FUS, and RBM14) for this tethering experiment. We expressed MS2 coat protein (MCP) fused with PSPs (e.g., MCP-NONO) in this cell line (Figures S6A and S6B). By expressing MCP-NONO, MCP-SFPQ, or MCP-FUS, paraspeckle formation was rescued in the m13–16.6k/6 × MS2BS cells (Figures 6B, left, 6E, and S6C). Neither negative control MCP-GFP-NLS nor MCP-RBM14 rescued paraspeckle formation. As controls, we expressed the MCP-fusion proteins in the parental m13–16.6k cells without 6 × MS2BS, but none of them rescued paraspeckle formation (Figures 6B, right, 6E, and S6C). SRM revealed that the paraspeckles rescued by the tethering possessed the properly ordered core-shell structure (Figure 6C). Treatment with 1,6-HD but not 2,5-HD disrupted the tethering-induced paraspeckles (Figure S6D). These data suggest that tethering of NONO, SFPQ, or FUS compensates for the lack of the functional NEAT1_2 subdomains and induces phase separation.

We next investigated which domains of NONO were essential for the rescue activity. Of the three proteins that rescued mini-paraspeckle formation by tethering to m13–16.6k cells, NONO was chosen because SFPQ was hardly detected in mini-paraspeckles (Figure S4A) and FUS exhibited nonspecific RNA-binding features as shown later (Figure 7B). We constructed MCP-tagged NONO mutants lacking the coiled-coil domain (NONOΔCC) essential for paraspeckle localization and intermolecular polymerization of NONO (Passon et al., 2012). We also made NONO lacking the NOPS domain (NONOΔNOPS), which is essential for dimer formation with DBHS family members (Passon et al., 2012), or PLD (NONOΔPLD) (Hennig et al., 2015) (Figures S6A and S6B). Tethering of MCP-NONO mutants revealed that NONOΔNOPS lost the rescue activity, whereas NONOΔCC and NONOΔPLD did not (Figures 6D and 6E). Since the NOPS domain is essential for dimer formation of two DBHS proteins (Passon et al., 2012), NONOΔNOPS is likely defective in interaction with endogenous NONO or other DBHS proteins such as SFPQ and PSPC1. To determine whether NOPS is required to interact with other DBHS proteins experimentally, we performed coIP using MCP-NONO WT, ΔNOPS, or ΔCC to examine the interactions with DBHS proteins (Figure 6F). As expected, MCP-NONO WT interacted with NONO, SFPQ, and PSPC1, whereas MCP-NONOΔNOPS did not. MCP-NONOΔCC still interacted with these proteins, although the interaction was weaker than with the WT. From these data, we argue that the actual function of the subdomains is to recruit NONO to form the primary dimers

(B and C) SRM observation of paraspeckles in WT and mini-NEAT1 cells. Indicated probes as shown in (A) were used. The cells were treated with 5 μM MG132 for 6 hr. Scale bar, 500 nm.

(D) Quantitation of NEAT1_2 levels in the WT and mini-NEAT1 by RT-qPCR (WT = 1). Data are represented as mean ± SD (n = 3).

(E) The model of NEAT1_2 configuration within paraspeckles in WT and mini-NEAT1 cells. 5′ and 3′ termini and middle region (mid) of NEAT1_2 are shown in the two-layered paraspeckle structure.

(F and G) EM observation of the paraspeckle structure in mini-NEAT1 cells. Localization of NONO and BRG1 (F), and the 5′ terminus and middle (D2) of NEAT1 in the paraspeckles bleached by proteinase K treatment (G). No MG132 treatment was performed in (F), whereas treatment with 5 μM MG132 for 17 hr was performed in (G). Scale bar, 100 nm in (F) and 200 nm in (G).

(H) Quantitation of paraspeckle sizes. The surface area (left), Sx diameter (middle), and Lx diameter (right) of paraspeckles in MG132-untreated WT and mini-NEAT1 cells are plotted (****$p < 0.0001$).

(I and J) Paraspeckles in HAP1 cells treated with 0%–10% 1,6-HD (I: WT, J: mini-NEAT1) observed by NEAT1 RNA-FISH using NEAT1_5′ probes (green) and by NONO IF (magenta). The cells were treated with 5 μM MG132 for 6 hr. Scale bar, 10 μm.

(K) SRM observation of paraspeckle substructures in HAP1 WT and mini-NEAT1 cells in the presence of 1,6-HD or 2,5-HD. Paraspeckle substructures are visualized by NEAT1 FISH with the mixture of NEAT1–5′ and NEAT1–3′ probes to detect the shell (green) and NONO IF to detect the core (magenta). The cells were treated with 5 μM MG132 for 6 hr. Scale bar, 500 nm.

(L) NONO immunoprecipitation under various washing conditions (upper panel). A CBB-stained SDS-PAGE gel image is shown (lower panels). Immunoblotting with indicated antibodies is shown. HS, high salt. Filled circles indicate proteins that show reduced binding to NONO proteins after washing with 1,6-HD.

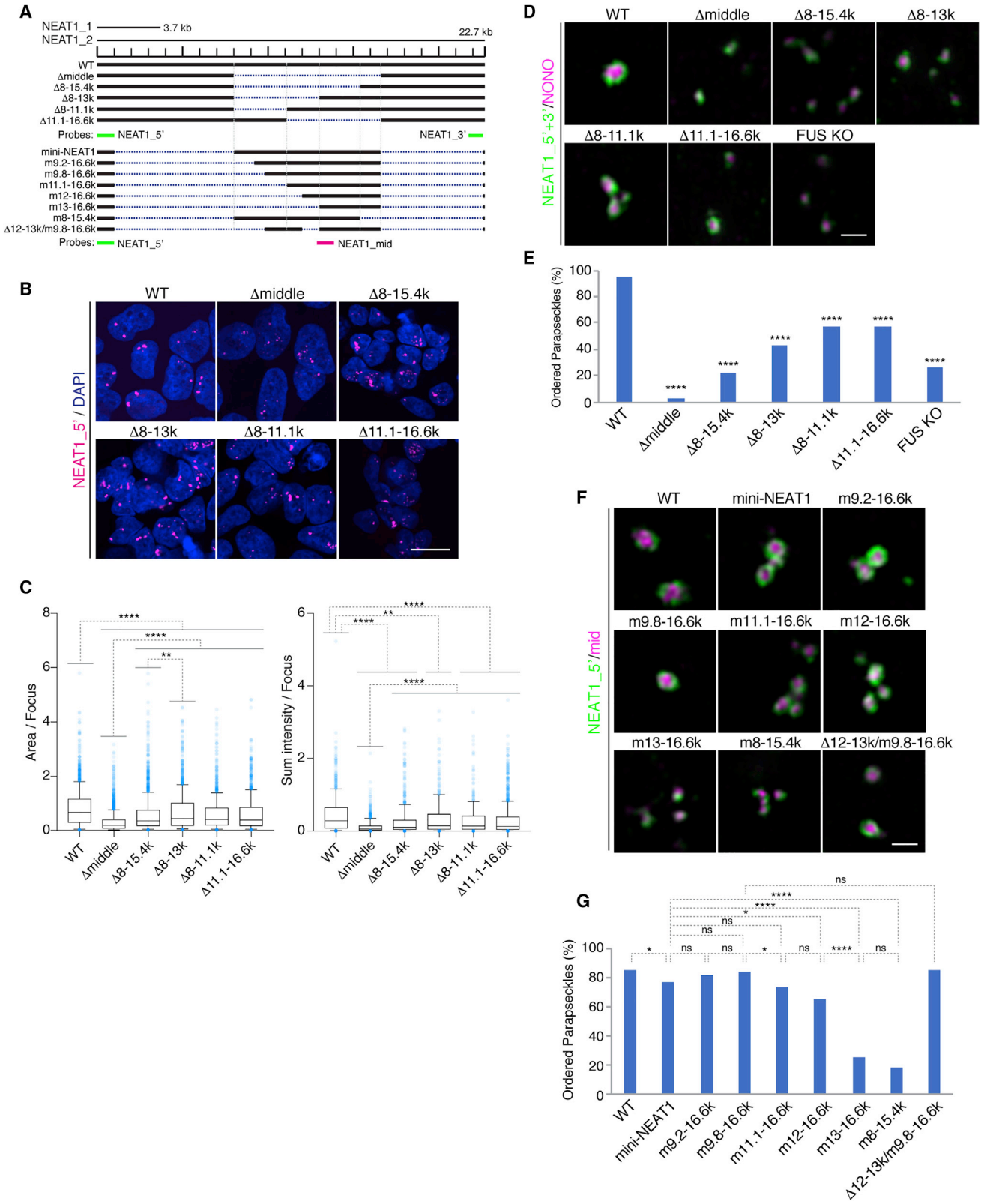

(legend on next page)

on NEAT1_2 that become the scaffold to initiate oligomerization with other PSPs to form the structure of massive paraspeckles.

NONO plays an essential role in paraspeckle formation by maintaining NEAT1_2 levels (Naganuma et al., 2012). The above data strongly suggest that NONO is also involved in the assembly of paraspeckles. In our previous experiments, NEAT1_2 and paraspeckle foci were undetectable after depletion of NONO (Naganuma et al., 2012); therefore, it was impossible to judge the requirement for NONO in the assembly step. However, we recently found that paraspeckle-like foci with substantial amounts of NEAT1_2 were detectable in MG132-treated NONO KO cells (ΔNONO), although they were much smaller than in WT cells (Figures S6E–S6H). SRM revealed that the paraspeckle-like foci in ΔNONO were structurally disordered (Figure S6I), suggesting that NONO has a distinct, essential function for assembly of the ordered paraspeckle structure.

RNA Fragments of the NEAT1_2 Subdomain Specifically Bind NONO and SFPQ, and Induce Higher-Order Assembly *In Vitro*

We next asked whether the identified NEAT1_2 subdomains (9.8–12 kb and 12–13 kb), deletion of which could be rescued by tethering NONO, SFPQ, or FUS, can interact with these proteins. We thus carried out *in vitro* RNA pull-down from nuclear extracts (NEs) using biotinylated sense or antisense RNA fragments of the NEAT1_2 subdomains. By Coomassie brilliant blue (CBB) staining of the co-precipitated proteins, specific proteins were precipitated with the sense RNAs but not with the antisense RNAs (Figure 7A). Immunoblotting analysis revealed that three essential PSPs (NONO, SFPQ, and RBM14) were specifically precipitated with the sense RNA. Interestingly, FUS nonspecifically bound both to the sense and antisense RNAs (Figure 7B). Next we investigated the binding preferences of PSPs for sense RNA fragments from the middle domain of NEAT1_2. CBB staining and immunoblotting revealed strong binding of NONO and SFPQ to 12- to 13-kb and 13- to 14-kb RNAs, which contain the functional subdomain and its adjacent domain, respectively (Figures 7C and 7D). Both proteins also bound substantially to other sense RNAs (Figure 7D). Moreover, UV cross-linking and immunoprecipitation (CLIP) sequencing (CLIP-seq) data indicated that NONO, SFPQ, and FUS bound numerous sites on NEAT1_2, some of which overlapped with the NEAT1_2 subdomains (Figure S7A). Together, these data strongly suggest that the binding preference of these PSPs with the sense RNA reflects the requirement of the NEAT1_2 subdomains for paraspeckle formation *in vivo*.

During the RNA pull-down experiments (Figure 7A), we often observed magnetic bead aggregates visible to the eye in the presence of NEAT1 12–13k sense RNAs (Figure S7B). This suggests the ability of the NEAT1_2 RNA fragments, which strongly bind NONO and SFPQ, to facilitate higher-order assembly *in vitro*. We quantified the bead aggregation by microscopy, which enabled us to detect single magnetic beads conjugated with RNAs (Figures S7C and S7D). Upon mixing 12–13k sense RNAs, but not 12–13k antisense RNAs, with nuclear extract (NE), large bead aggregates formed (Figure 7E). Importantly, without NE, 12–13k sense RNAs themselves did not induce bead aggregates (Figure 7E), suggesting that proteins interacting with the sense RNAs are required for the aggregate formation. When we used washing buffer containing 10% 1,6-HD, the aggregates were disrupted and the size of the aggregates induced by the sense and antisense RNAs became similar (Figure 7E). In addition, we washed the beads with washing buffer containing 10% 2,5-HD and clearly observed much larger aggregates in the presence of sense RNAs than antisense RNAs (Figure 7E), suggesting that the proteins dissociated by 1,6-HD washing are involved in the aggregation. We thus examined the binding proteins in these conditions. CBB staining clearly showed a loss of protein binding to the 12–13k sense RNAs after washing with 1,6-HD, but not with 2,5-HD (Figure 7F). NONO, SFPQ, RBM14, and FUS were dissociated from the beads, although FUS dissociation was less prominent than dissociation of the other proteins (Figure 7F). Specific depletion of NONO/SFPQ dimers from NE (Δ in Figures 7G and S7E) resulted in loss of interactions between these proteins and 12–13k sense RNA (Figure 7G) and significant reduction in bead aggregate size (Figure 7H). Despite the presence of RBM14 and FUS in ΔNE, they could not bind to 12–13k sense RNA (Figure 7G), suggesting that NONO/SFPQ are required for binding of RBM14 and FUS to 12–13k sense RNA. These data strongly suggest that the RNA fragments of NEAT1_2 subdomains can induce higher-order assembly *in vitro* by recruiting proteins including essential PSPs.

DISCUSSION

We established various NEAT1 deletion mutant lines and revealed the modular domain structure of the NEAT1 lncRNA.

Figure 5. NEAT1_2 Middle Domain Contains Multiple Redundant Subdomains for Paraspeckle Assembly

(A) The schematics of the WT and five deletion mutants of the NEAT1_2 middle domain (upper), as well as those of the WT and eight deletion mutants derived from mini-NEAT1 mutants (lower), are shown with a scale. The positions of the NEAT1_5′ (green line), NEAT1_3′ (green line), and NEAT1_mid (magenta line) antisense probes for SRM are shown below.

(B) Observation of the paraspeckles in the cell in (A) with the NEAT1_5′ (magenta) smFISH probe. The cells were treated with 5 μM MG132 for 6 hr. Scale bar, 10 μm.

(C) Quantitation of the paraspeckle sizes observed in (B) (****$p < 0.0001$, **$p < 0.01$, unindicated pairs were not significantly different).

(D) SRM observation of shell and core substructure of paraspeckles in the WT, the five mutants in (A), and FUS KO cells. Paraspeckle substructures are visualized by NEAT1 FISH with the mixture of NEAT1_5′ and NEAT1_3′ probes to detect the shell (green) and NONO IF to detect the core (magenta). The cells were treated with 5 μM MG132 for 6 hr.

(E) Ratio (%) of paraspeckles with ordered structure in the cells observed in (D) (****$p < 0.0001$, compared with the WT).

(F) SRM observation of the paraspeckles in the WT and the eight mutants shown in (A). For RNA-FISH, NEAT1_5′ (green) and NEAT1_mid (magenta) were used as shown on the left. The cells were treated with 5 μM MG132 for 6 hr. Scale bar, 500 nm.

(G) Ratio (%) of paraspeckles with ordered structure in the cells observed in (G) (****$p < 0.0001$, *$p < 0.05$; ns, not significant).

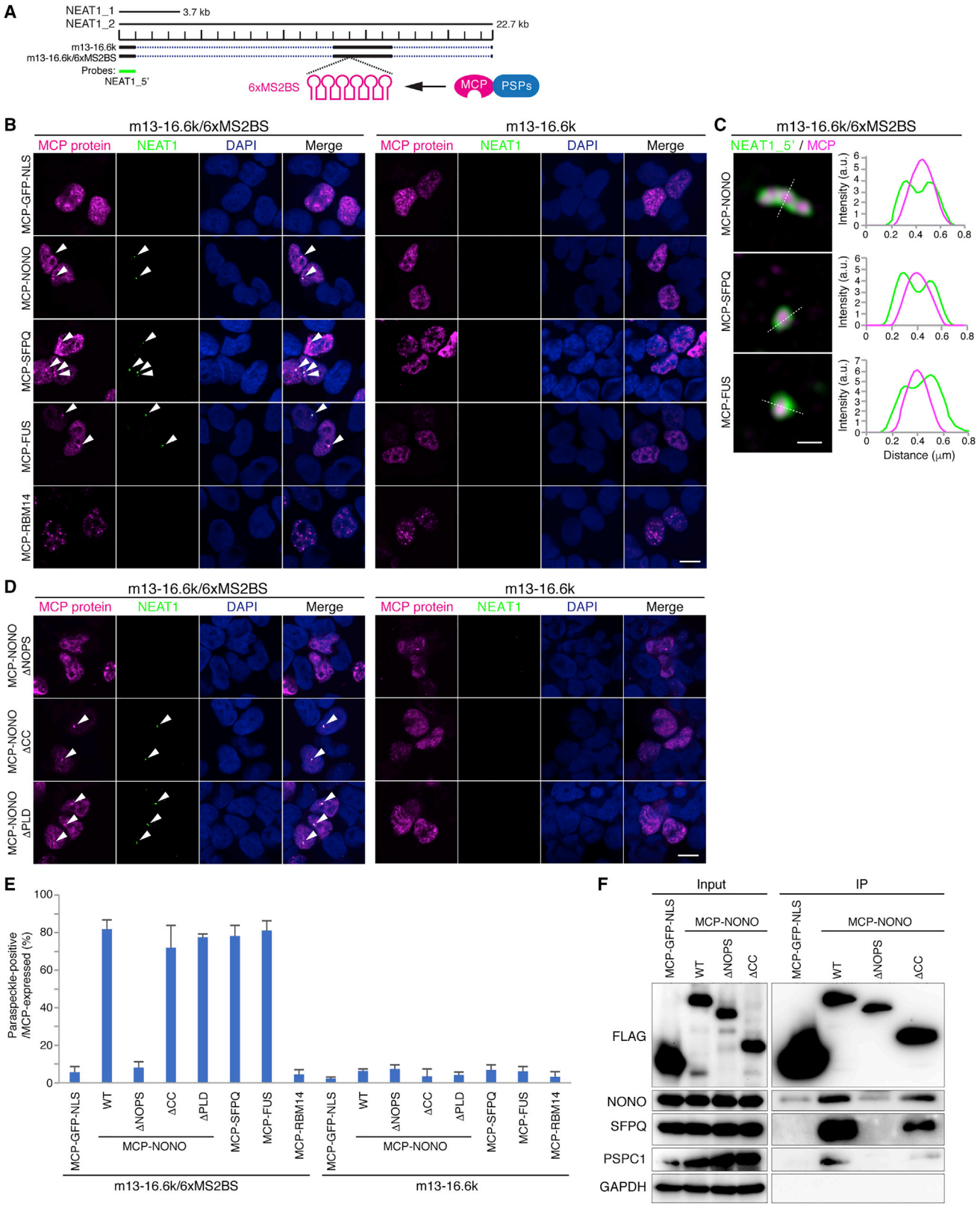

(legend on next page)

Our strategy combining CRISPR/Cas9 technology and HAP1 haploid cells is a powerful one to efficiently establish unambiguous targeted deletions. We found that the 5′ terminal domain (0–1 kb) and the 3′ TH are both required for stabilization of NEAT1_2. The decay rate of NEAT1_2 in Δ0–1k cells was more moderate than that in ΔTH, suggesting that the 0–1k domain is required not only for RNA stability but also for efficient transcription. The locations of these functional domains are consistent with the configuration of NEAT1_2 molecules in paraspeckles; both NEAT1_2 termini are located at the surface of the body where they can be exposed to attacks by exoribonucleases, and the middle part of NEAT1_2 that initiates paraspeckle formation is located in the interior core.

The middle domain (8–16.6 kb) is sufficient for paraspeckle assembly and contains at least three functional subdomains (C1: 9.8–12k, C2: 12–13k, and C3: 15.4–16.6k) (Figure 7I). Based on the analysis using deletion mutants derived from mini-NEAT1, deletion of C1 and C2 abolished the paraspeckle assembly. However, sole deletion of C1 or C2 did not abolish paraspeckle assembly, indicating that C1 and C2 act redundantly. On the other hand, C3 might be a distinct functional subdomain since the sole deletion of C3 abolished the function of mini-NEAT1. Similar redundancy in the function of the middle domain is also exerted by the regions outside of the middle domain, as suggested from comparison of the phenotype of deletion mutants constructed from mini-NEAT1 and those from the WT (Figure 5A). Remarkably, deletion of the C3 subdomain (15.4–16.6k) from the WT did not affect paraspeckle integrity, whereas its deletion from mini-NEAT1 did (Figures S2A and S2B). Both Δ8–13k and m13–16.6k lacked the essential region including the C1 and C2 subdomains, and m13–16.6k showed a more severe defective phenotype (<20%) than that in Δ8–13k (>40%) (Figures 5E and 5G). Thus, there are multiple functional redundancies between the middle domain and the outside region, as well as within the middle domain.

The functional subdomains in the middle domain are required for the assembly step in which some of the essential PSPs likely interact to dictate the function. Indeed, tethering of NONO, SFPQ, or FUS but not RBM14 to m13–16.6k rescued paraspeckle assembly, strongly suggesting that the C2 subdomain, which binds essential PSPs including NONO and SFPQ *in vitro* and *in vivo*, shows an ability to facilitate higher-order assembly *in vitro* and functionally recruits these PSPs to initiate paraspeckle assembly. Tethering of mutant NONO showed that the rescue activity requires the NOPS domain, which is required for dimerization with the DBHS proteins (Passon et al., 2012). Interestingly, tethering of mutant NONO lacking the CC maintains the rescue activity even though the CC is required for the polymerization of NONO that likely underlies paraspeckle assembly. Considering that endogenous WT NONO coexists in the cells, the main function of the NEAT1_2 subdomain is likely to recruit and form NONO dimers with other DBHS proteins such as SFPQ. The subsequent polymerization, which is one of the distinct characteristics of DBHS proteins, can be conducted via the CC of the endogenous NONO in the primary dimer interacting with the C1 and C2 subdomains (Figure 7I). RNA fragments derived from the C2 subdomain and its adjacent region preferentially bound NONO and SFPQ (Figure 7D), suggesting that the subdomain is enriched for sequence stretches with affinity for PSPs. The other parts of the middle domain including the C1 and C3 subdomains exhibited lower but substantial affinity for NONO and SFPQ (Figure 7D). Photoactivatable ribonucleoside-enhanced cross-linking and immunoprecipitation (PAR-CLIP) data indicate that PSP-binding sites broadly cover the whole NEAT1_2 region, and that the C2 subdomain contains multiple prominent binding peaks for NONO and SFPQ (Figure S7A). The difference between the preferential binding sites in the C2 subdomain and other scattered binding sites remains to be elucidated. An intriguing possibility is that the identified subdomains are primary binding sites of PSPs that act as seeds to spread PSPs throughout the broad NEAT1_2 region via their polymerization described above (Figure 7I). In support of this idea, a previous study using transmission EM showed that SFPQ can coat DNA to form higher-order complexes by polymerization through the CC domain (Lee et al., 2015). As another example, cooperative spreading of HNRNPA1 on pre-mRNA carrying high-affinity binding sites was previously reported (Zhu et al., 2001). In addition, our bead aggregation assay supports the idea that the oligomerization of NEAT1 ribonucleoproteins (RNPs) occurs through the ability of NEAT1_2 subdomains to recruit essential PSPs including NONO and SFPQ. Moreover, LLPS is likely to be the driving force for paraspeckle formation for three reasons: (1) paraspeckles are sensitive to 1,6-HD treatment in a similar manner to LLPS-formed Cajal bodies, (2) FUS and RBM14 PLDs cause *in vitro* hydrogel formation and are required for *in vivo* paraspeckle formation (Hennig et al., 2015), and (3) PSPs rapidly move into and out of the paraspeckle (Fox et al., 2002; Mao et al., 2011), and thus the paraspeckle is highly dynamic, which is one of the characteristics of phase-separated bodies. We found that the tethering of FUS can rescue

Figure 6. An Essential NEAT1_2 Subdomain for Mini-paraspeckle Formation Can Be Functionally Replaced by Artificially Tethered Essential PSPs

(A) The schematics of the m13–16.6k mutant with or without 6 × MS2BS for MCP-PSP tethering experiments. The position of the NEAT1_5′ probe used is shown below.

(B) Observation of paraspeckle formation with transfection of MCP-PSPs into m13–16.6k/6 × MS2BS (left panels) or m13–16.6k cells (right panels) in the MG132 treatment condition (5 μM for 6 hr). The rescued paraspeckles, which are visualized by IF of MCP protein with αFlag antibody (magenta) and NEAT1 FISH (green), are indicated by white arrowheads. Scale bar, 10 μm.

(C) SRM observation of the rescued paraspeckles with MCP-NONO, MCP-SFPQ, and MCP-FUS corresponding to the results in (B). Paraspeckle substructures were visualized by NEAT1 FISH (green) and MCP IF (magenta). Scale bar, 500 nm.

(D) Tethering of the MCP-tagged mutant NONO lacking NOPS, CC, or PLD domains as in Figure 6B. Scale bar, 10 μm.

(E) Quantitation of the cells with rescued paraspeckles in (B) and (D). Data are represented as mean ± SD (n = 3).

(F) Coimmunoprecipitation of MCP-NONO, ΔNOPS, and ΔCC mutants with a control, MCP-GFP-NLS. Immunoblotting was performed to detect DBHS proteins in the coIP samples. GAPDH served as a negative control.

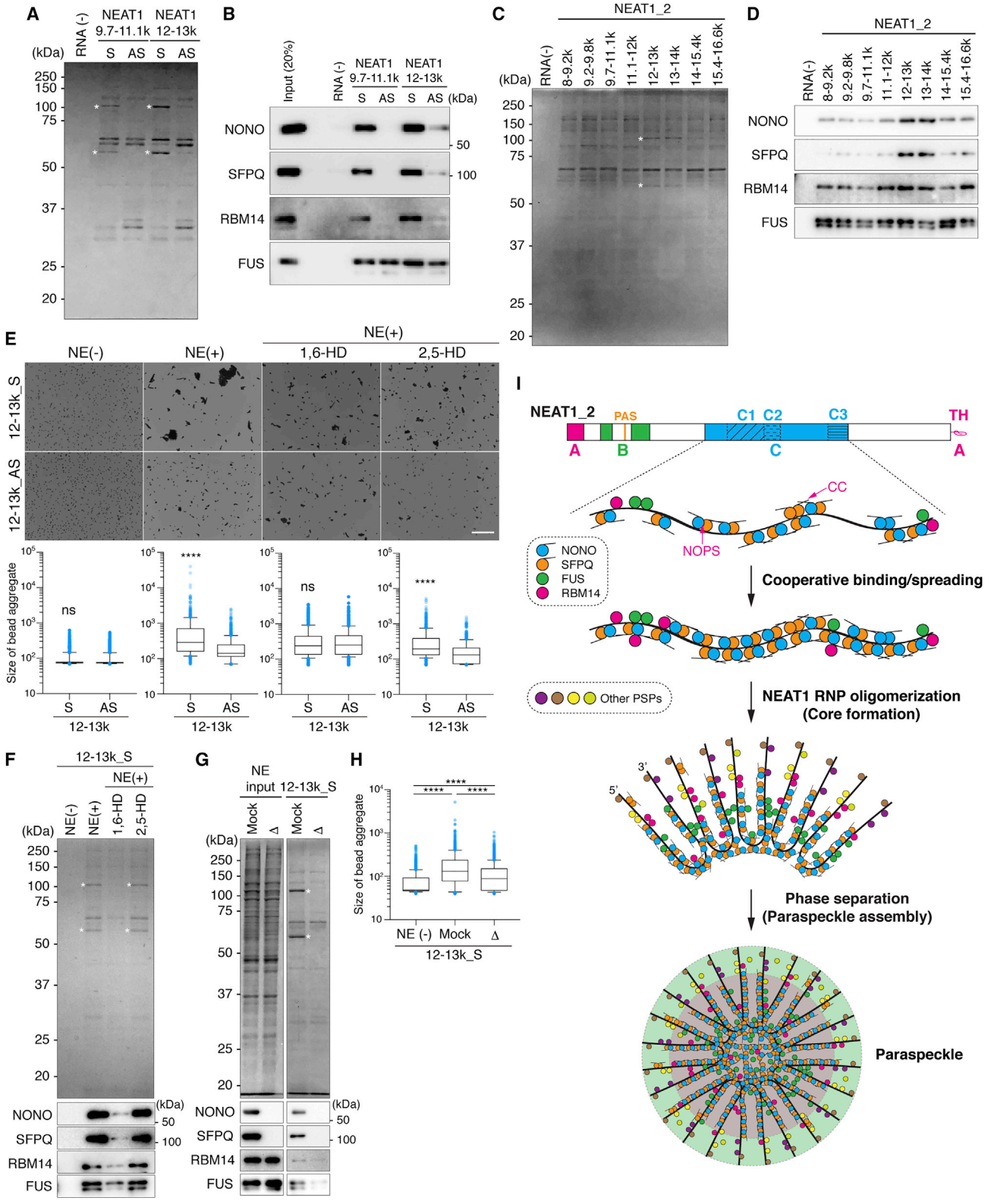

(legend on next page)

paraspeckle formation in the m13–16.6k mutant. Since the PLD of FUS is required for paraspeckle assembly and phase separation, the tethered FUS might recruit multiple PSPs and/or form FUS oligomers through its PLD, leading to paraspeckle assembly via phase separation. Consistently, we found that treatment with concentrations of 1,6-HD that disrupted paraspeckle structure also disturbed interactions between NONO and the RNA binding proteins with PLDs including FUS (Figure 4L).

Several reports indicate the importance of multivalent interactions in phase separation (Banani et al., 2017; Shin and Brangwynne, 2017). As discussed above, multiple redundant NEAT1_2 middle domains including the identified functional subdomains likely serve as multiple binding sites for essential PSPs including DBHS proteins (e.g., NONO and SFPQ) and proteins with PLDs (e.g., FUS and RBM14), which have an ability for multivalent interactions. For example, DBHS proteins can bind RNAs via RNA recognition motifs (RRMs), dimerize via the NOPS domain, and reversibly polymerize via the CC domain (Knott et al., 2016). In addition, the PLD promotes multivalent and transient interactions (Kroschwald et al., 2015). Recently, RNA self-assembly was shown to contribute to formation of phase-separated stress granules (Van Treeck et al., 2018), raising the intriguing possibility that self-assembly of NEAT1 at its transcription site may contribute to paraspeckle integrity. Therefore, it appears that various multivalent interactions between RNAs and proteins, and proteins and proteins, through NOPS, CC, and PLD, and presumably via self-assembly of NEAT1, contribute to the formation of this massive, dynamic, highly ordered NB. It is tempting to speculate that the NEAT1 domains redundantly required for paraspeckle assembly reduce a critical NEAT1 concentration threshold for phase separation to form paraspeckles.

NEAT1_2 shows a characteristic spatial organization within the paraspeckle. Our observation of aberrant localization of the 3′ terminus of mini-NEAT1 to the core of the paraspeckle suggests the presence of NEAT1 subdomain required for NEAT1_2 spatial organization (Figure 4E). Further, NEAT1_2 deletion analysis suggested that the 16.6- to 22.6-kb region, which is distinct from the paraspeckle assembly domain, is required for shell localization of NEAT1_2 3′ terminus (Figures S4B–S4E). This observation will facilitate further research into the biological functions of paraspeckles related to NEAT1_2 spatial organization. Although we revealed several NEAT1 functional domains, NEAT1 likely possesses additional domains required for other biological functions. Since the number of reports on the normal and disease-related functions of NEAT1 is increasing, our mutant HAP1 cell lines will be a valuable resource to investigate further the links between NEAT1 domains and these functions.

A number of arcRNAs have been reported in various eukaryotic species (Chujo et al., 2016). Using two different approaches, we recently found additional arcRNA candidates as well as NBs built on putative arcRNAs (Chujo et al., 2017; Mannen et al., 2016). Data on the characterized arcRNAs raise the intriguing possibility of a common molecular mechanism underlying arcRNA function (Chujo et al., 2016). Here, we showed that multiple redundant NEAT1_2 subdomains provide the scaffold for paraspeckle assembly by recruiting NONO dimers that initiate oligomerization of DBHS proteins leading to massive RNP complex formation via phase separation (Figure 7I). It is also possible that other arcRNAs recruit distinct sets of RBPs that induce phase separation through their repetitive sequences. Indeed, the C3 subdomain overlaps with a repetitive sequence that is strongly bound by NONO and SFPQ *in vivo* (Figures S3B and S7A). In addition, the C1 subdomain, which interacts with SFPQ and NONO *in vitro* and *in vivo*, contains several highly similar repetitive sequences (Figures S3B, 7A, 7B, and S7A). Thus, it may be interesting to investigate the combination of RBPs and RNA domains that can efficiently induce phase separation, which would enable us to design arcRNAs using the modular RNA domains. Such fundamental understanding of RNA domains and functional machineries will lead us to deeper understandings of the mechanism, biological roles, and evolution of RNA-instructed architecture of subcellular structures.

STAR★METHODS

Detailed methods are provided in the online version of this paper and include the following:

- KEY RESOURCES TABLE
- CONTACT FOR REAGENT AND RESOURCE SHARING
- EXPERIMENTAL MODEL AND SUBJECT DETAILS
  - HAP1 cell line
- METHOD DETAILS
  - Plasmids

Figure 7. NEAT1_2 Middle Fragments Specifically Bind NONO and SFPQ and Induce Higher-Order Assembly *In Vitro*

(A and B) *In vitro* RNA pull-down to capture the associated proteins with the RNA fragments derived from the functional NEAT1_2 subdomains. The captured proteins were separated by SDS-PAGE and visualized by CBB staining. Asterisks indicate major interacting proteins specific to sense RNAs (A). Four essential PSPs were detected by immunoblotting (B).

(C and D) *In vitro* RNA pull-down with various NEAT1_2 middle RNA fragments. CBB-stained SDS-PAGE gel image (C) and immunoblotting analysis of the samples (D) are shown.

(E) Bead aggregation assay. Magnetic beads were observed by microscopy (upper panels). Quantification of bead aggregate sizes is shown in the lower panels. It should be noted that 10% 1,6-HD and 2,5-HD moderately affected bead aggregation presumably due to the indirect effects of these reagents in NE. Scale bar, 100 μm (****$p < 0.0001$; ns, not significant).

(F) (upper panel) CBB staining analysis of bound proteins on RNAs used in Figure 7E. Asterisks indicate major interacting proteins specific to sense RNAs. (lower panels) Immunoblotting analysis of the samples shown in the upper panel.

(G) Bead aggregation assay with NONO/SFPQ depleted (Δ) NE. Upper panels show CBB-stained SDS-PAGE gels and lower panels show immunoblotting analysis of the samples shown in the upper panel. (left) NE input samples of mock and Δ NE. Asterisks indicate major interacting proteins in pull-down samples with the mock depleted NE.

(H) Quantification of bead aggregate sizes in the experiment shown in Figure 7G (****$p < 0.0001$).

(I) The updated model for the construction of phase-separated paraspeckles with NEAT1 domains and PSPs (see text for details).

- Genome editing using CRISPR/Cas9
- Plasmid transfection
- RNA-FISH and immunofluorescence
- Single-molecule FISH (smFISH)
- Reverse transcription-quantitative PCR (RT-qPCR)
- RNase protection assay (RPA)
- 5-bromouridine pulse-chase analysis
- Immunoblotting
- Electron microscopy
- PAR-CLIP and mapping of CLIP-seq data
- Immunoprecipitation
- RNA pull-down
- Bead aggregation assay
- Affinity depletion from NE

- QUANTIFICATION AND STATISTICAL ANALYSIS
- DATA AND SOFTWARE AVAILABILITY

SUPPLEMENTAL INFORMATION

Supplemental Information includes seven figures and two tables and can be found with this article online at https://doi.org/10.1016/j.molcel.2018.05.019.

ACKNOWLEDGMENTS

The authors thank C. Fujikawa, A. Kubota, E. Fortini, A. Takahashi, J. Iwakiri, and T. Mannen for technical support and the members of the Hirose laboratory for valuable discussions. This research was supported by grants from the Ministry of Education, Culture, Sports, Science, and Technology of Japan (to T.Y. [26891001, 15K18474, and 17K15058], T.C. [15J01473 and 17K15084], and T.H. [26113002, 16H06279, 17H03630, and 17K19335]) and by a grant of the Joint Research Program of IGM, Hokkaido University (to A.H.F., S.N., G.P., and T.H.).

AUTHOR CONTRIBUTIONS

T.Y. and T.H. conceived and designed this study. T.Y. conducted most of the experiments. S.S. and G.P. performed EM analyses. T.C. performed RPA and immunoblotting. A.H.F., S.K., C.S.B., and Y.S.C. provided the PAR-CLIP data and related information. S.N. technically supported SRM. T.Y., T.C., and T.H. wrote the manuscript.

DECLARATION OF INTERESTS

The authors declare no competing interests.

Received: December 27, 2017
Revised: April 18, 2018
Accepted: May 16, 2018
Published: June 21, 2018

REFERENCES

Adriaens, C., Standaert, L., Barra, J., Latil, M., Verfaillie, A., Kalev, P., Boeckx, B., Wijnhoven, P.W., Radaelli, E., Vermi, W., et al. (2016). p53 induces formation of NEAT1 lncRNA-containing paraspeckles that modulate replication stress response and chemosensitivity. Nat. Med. *22*, 861–868.

Banani, S.F., Lee, H.O., Hyman, A.A., and Rosen, M.K. (2017). Biomolecular condensates: Organizers of cellular biochemistry. Nat. Rev. Mol. Cell Biol. *18*, 285–298.

Chen, L.L., and Carmichael, G.G. (2009). Altered nuclear retention of mRNAs containing inverted repeats in human embryonic stem cells: Functional role of a nuclear noncoding RNA. Mol. Cell *35*, 467–478.

Chu, C., Zhang, Q.C., da Rocha, S.T., Flynn, R.A., Bharadwaj, M., Calabrese, J.M., Magnuson, T., Heard, E., and Chang, H.Y. (2015). Systematic discovery of Xist RNA binding proteins. Cell *161*, 404–416.

Chujo, T., Yamazaki, T., and Hirose, T. (2016). Architectural RNAs (arcRNAs): A class of long noncoding RNAs that function as the scaffold of nuclear bodies. Biochim. Biophys. Acta *1859*, 139–146.

Chujo, T., Yamazaki, T., Kawaguchi, T., Kurosaka, S., Takumi, T., Nakagawa, S., and Hirose, T. (2017). Unusual semi-extractability as a hallmark of nuclear body-associated architectural noncoding RNAs. EMBO J. *36*, 1447–1462.

Clemson, C.M., Hutchinson, J.N., Sara, S.A., Ensminger, A.W., Fox, A.H., Chess, A., and Lawrence, J.B. (2009). An architectural role for a nuclear noncoding RNA: NEAT1 RNA is essential for the structure of paraspeckles. Mol. Cell *33*, 717–726.

Engreitz, J.M., Ollikainen, N., and Guttman, M. (2016). Long non-coding RNAs: Spatial amplifiers that control nuclear structure and gene expression. Nat. Rev. Mol. Cell Biol. *17*, 756–770.

Fox, A.H., Lam, Y.W., Leung, A.K., Lyon, C.E., Andersen, J., Mann, M., and Lamond, A.I. (2002). Paraspeckles: A novel nuclear domain. Curr. Biol. *12*, 13–25.

Hafner, M., Landthaler, M., Burger, L., Khorshid, M., Hausser, J., Berninger, P., Rothballer, A., Ascano, M., Jr., Jungkamp, A.C., Munschauer, M., et al. (2010). Transcriptome-wide identification of RNA-binding protein and microRNA target sites by PAR-CLIP. Cell *141*, 129–141.

Hennig, S., Kong, G., Mannen, T., Sadowska, A., Kobelke, S., Blythe, A., Knott, G.J., Iyer, K.S., Ho, D., Newcombe, E.A., et al. (2015). Prion-like domains in RNA binding proteins are essential for building subnuclear paraspeckles. J. Cell Biol. *210*, 529–539.

Hirose, T., Virnicchi, G., Tanigawa, A., Naganuma, T., Li, R., Kimura, H., Yokoi, T., Nakagawa, S., Bénard, M., Fox, A.H., and Pierron, G. (2014). NEAT1 long noncoding RNA regulates transcription via protein sequestration within subnuclear bodies. Mol. Biol. Cell *25*, 169–183.

Kawaguchi, T., Tanigawa, A., Naganuma, T., Ohkawa, Y., Souquere, S., Pierron, G., and Hirose, T. (2015). SWI/SNF chromatin-remodeling complexes function in noncoding RNA-dependent assembly of nuclear bodies. Proc. Natl. Acad. Sci. USA *112*, 4304–4309.

Knott, G.J., Bond, C.S., and Fox, A.H. (2016). The DBHS proteins SFPQ, NONO and PSPC1: A multipurpose molecular scaffold. Nucleic Acids Res. *44*, 3989–4004.

Kroschwald, S., Maharana, S., Mateju, D., Malinovska, L., Nüske, E., Poser, I., Richter, D., and Alberti, S. (2015). Promiscuous interactions and protein disaggregases determine the material state of stress-inducible RNP granules. eLife *4*, e06807.

Lee, K.A., and Green, M.R. (1990). Small-scale preparation of extracts from radiolabeled cells efficient in pre-mRNA splicing. Methods Enzymol. *181*, 20–30.

Lee, M., Sadowska, A., Bekere, I., Ho, D., Gully, B.S., Lu, Y., Iyer, K.S., Trewhella, J., Fox, A.H., and Bond, C.S. (2015). The structure of human SFPQ reveals a coiled-coil mediated polymer essential for functional aggregation in gene regulation. Nucleic Acids Res. *43*, 3826–3840.

Lin, Y., Mori, E., Kato, M., Xiang, S., Wu, L., Kwon, I., and McKnight, S.L. (2016). Toxic PR poly-dipeptides encoded by the C9orf72 repeat expansion target LC domain polymers. Cell *167*, 789–802.

Mannen, T., Yamashita, S., Tomita, K., Goshima, N., and Hirose, T. (2016). The Sam68 nuclear body is composed of two RNase-sensitive substructures joined by the adaptor HNRNPL. J. Cell Biol. *214*, 45–59.

Mao, Y.S., Sunwoo, H., Zhang, B., and Spector, D.L. (2011). Direct visualization of the co-transcriptional assembly of a nuclear body by noncoding RNAs. Nat. Cell Biol. *13*, 95–101.

Naganuma, T., Nakagawa, S., Tanigawa, A., Sasaki, Y.F., Goshima, N., and Hirose, T. (2012). Alternative 3′-end processing of long noncoding RNA initiates construction of nuclear paraspeckles. EMBO J. *31*, 4020–4034.

Nakagawa, S., Shimada, M., Yanaka, K., Mito, M., Arai, T., Takahashi, E., Fujita, Y., Fujimori, T., Standaert, L., Marine, J.C., and Hirose, T. (2014). The

lncRNA Neat1 is required for corpus luteum formation and the establishment of pregnancy in a subpopulation of mice. Development *141*, 4618–4627.

Passon, D.M., Lee, M., Rackham, O., Stanley, W.A., Sadowska, A., Filipovska, A., Fox, A.H., and Bond, C.S. (2012). Structure of the heterodimer of human NONO and paraspeckle protein component 1 and analysis of its role in subnuclear body formation. Proc. Natl. Acad. Sci. USA *109*, 4846–4850.

Quinn, J.J., and Chang, H.Y. (2016). Unique features of long non-coding RNA biogenesis and function. Nat. Rev. Genet. *17*, 47–62.

Ran, F.A., Hsu, P.D., Wright, J., Agarwala, V., Scott, D.A., and Zhang, F. (2013). Genome engineering using the CRISPR-Cas9 system. Nat. Protoc. *8*, 2281–2308.

Sanjana, N.E., Shalem, O., and Zhang, F. (2014). Improved vectors and genome-wide libraries for CRISPR screening. Nat. Methods *11*, 783–784.

Sasaki, Y.T., Ideue, T., Sano, M., Mituyama, T., and Hirose, T. (2009). MENepsilon/beta noncoding RNAs are essential for structural integrity of nuclear paraspeckles. Proc. Natl. Acad. Sci. USA *106*, 2525–2530.

Shin, Y., and Brangwynne, C.P. (2017). Liquid phase condensation in cell physiology and disease. Science *357*. . Published online September 22, 2017. https://doi.org/10.1126/science.aaf4382.

Snijders, A.P., Hautbergue, G.M., Bloom, A., Williamson, J.C., Minshull, T.C., Phillips, H.L., Mihaylov, S.R., Gjerde, D.T., Hornby, D.P., Wilson, S.A., et al. (2015). Arginine methylation and citrullination of splicing factor proline- and glutamine-rich (SFPQ/PSF) regulates its association with mRNA. RNA *21*, 347–359.

Souquere, S., and Pierron, G. (2015). Ultrastructural analysis of nuclear bodies using electron microscopy. Methods Mol. Biol. *1262*, 105–118.

Souquere, S., Beauclair, G., Harper, F., Fox, A., and Pierron, G. (2010). Highly ordered spatial organization of the structural long noncoding NEAT1 RNAs within paraspeckle nuclear bodies. Mol. Biol. Cell *21*, 4020–4027.

Staněk, D., and Fox, A.H. (2017). Nuclear bodies: News insights into structure and function. Curr. Opin. Cell Biol. *46*, 94–101.

Sunwoo, H., Dinger, M.E., Wilusz, J.E., Amaral, P.P., Mattick, J.S., and Spector, D.L. (2009). MEN epsilon/beta nuclear-retained non-coding RNAs are up-regulated upon muscle differentiation and are essential components of paraspeckles. Genome Res. *19*, 347–359.

Tollervey, J.R., Curk, T., Rogelj, B., Briese, M., Cereda, M., Kayikci, M., König, J., Hortobágyi, T., Nishimura, A.L., Zupunski, V., et al. (2011). Characterizing the RNA targets and position-dependent splicing regulation by TDP-43. Nat. Neurosci. *14*, 452–458.

Van Treeck, B., Protter, D.S.W., Matheny, T., Khong, A., Link, C.D., and Parker, R. (2018). RNA self-assembly contributes to stress granule formation and defining the stress granule transcriptome. Proc. Natl. Acad. Sci. USA *115*, 2734–2739.

Visa, N., Puvion-Dutilleul, F., Bachellerie, J.P., and Puvion, E. (1993). Intranuclear distribution of U1 and U2 snRNAs visualized by high resolution in situ hybridization: Revelation of a novel compartment containing U1 but not U2 snRNA in HeLa cells. Eur. J. Cell Biol. *60*, 308–321.

West, J.A., Mito, M., Kurosaka, S., Takumi, T., Tanegashima, C., Chujo, T., Yanaka, K., Kingston, R.E., Hirose, T., Bond, C., et al. (2016). Structural, super-resolution microscopy analysis of paraspeckle nuclear body organization. J. Cell Biol. *214*, 817–830.

Wilusz, J.E., JnBaptiste, C.K., Lu, L.Y., Kuhn, C.D., Joshua-Tor, L., and Sharp, P.A. (2012). A triple helix stabilizes the 3′ ends of long noncoding RNAs that lack poly(A) tails. Genes Dev. *26*, 2392–2407.

Wutz, A., Rasmussen, T.P., and Jaenisch, R. (2002). Chromosomal silencing and localization are mediated by different domains of Xist RNA. Nat. Genet. *30*, 167–174.

Yamazaki, T., and Hirose, T. (2015). The building process of the functional paraspeckle with long non-coding RNAs. Front. Biosci. (Elite Ed.) *7*, 1–41.

Yamazaki, T., Chen, S., Yu, Y., Yan, B., Haertlein, T.C., Carrasco, M.A., Tapia, J.C., Zhai, B., Das, R., Lalancette-Hebert, M., et al. (2012). FUS-SMN protein interactions link the motor neuron diseases ALS and SMA. Cell Rep. *2*, 799–806.

Zhou, Y., Liu, S., Liu, G., Oztürk, A., and Hicks, G.G. (2013). ALS-associated FUS mutations result in compromised FUS alternative splicing and autoregulation. PLoS Genet. *9*, e1003895.

Zhu, J., Mayeda, A., and Krainer, A.R. (2001). Exon identity established through differential antagonism between exonic splicing silencer-bound hnRNP A1 and enhancer-bound SR proteins. Mol. Cell *8*, 1351–1361.

STAR★METHODS

KEY RESOURCES TABLE

REAGENT or RESOURCE	SOURCE	IDENTIFIER
Antibodies		
Mouse monoclonal anti-NONO (clone 3/p54nrb)	BD Biosciences	Cat#611279
Mouse monoclonal anti-NONO (for PAR-CLIP)	Souquere et al. 2010	N/A
Mouse monoclonal anti-FUS (clone 4H11)	Santa Cruz Biotechnology	Cat#sc-47711
Mouse monoclonal anti-SFPQ (PSF) (clone C23)	MBL	Cat#RN014MW
Rabbit polyclonal anti-RBM14	Bethyl Laboratories	Cat#A300-331A
Rabbit polyclonal anti-PSPC1	Naganuma et al., 2012	N/A
Rabbit polyclonal anti-BRG1	Bethyl Laboratories	Cat#A300-813A
Mouse monoclonal anti-FLAG (clone M2)	Sigma-Aldrich	Cat#F3165
Rabbit polyclonal anti-GAPDH	Abcam	Cat#ab37168
Mouse monoclonal anti-Digoxigenin (clone 21H8)	Abcam	Cat#ab420
Rabbit polyclonal anti-Fluorescein	Abcam	Cat#ab19491
Anti-mouse IgG, Cy2 conjugate	Abcam	Cat#ab6944
Goat anti-rabbit IgG, Cy2 conjugate	Abcam	Cat#ab6940
Goat anti-mouse IgG, Cy3 conjugate	Merck	Cat#AP124C
Anti-rabbit IgG, Cy3 conjugate	Merck	Cat#AP132C
Anti-mouse IgG, Alexa 488 conjugate	Thermo Fisher Scientific	Cat#A-11029
Anti-rabbit IgG, Alexa 488 conjugate	Thermo Fisher Scientific	Cat#A-11034
Anti-mouse IgG, Alexa 568 conjugate	Thermo Fisher Scientific	Cat#A-11031
Anti-rabbit IgG, Alexa 568 conjugate	Thermo Fisher Scientific	Cat#A-11036
Anti-mouse IgG antibody coupled to 10-nm gold particles	TebuBio	Cat#EM.GMHL10
Anti-rabbit IgG antibody coupled to 10-nm gold particles	TebuBio	Cat#EM.GAR10
Goat anti-biotin antibody conjugated to 10nm gold particles	TebuBio	Cat#EM.GAB10
Bacterial and Virus Strains		
DH5α Competent Cells	Thermo Fisher Scientific	Cat#18265017
Chemicals, Peptides, and Recombinant Proteins		
Z-Leu-Leu-Leu-al (MG132)	Sigma-Aldrich	Cat#C2211
5,6-Dichlorobenzimidazole 1-β-D-ribofuranoside (DRB)	Sigma-Aldrich	Cat#D1916
Blasticidin	InvivoGen	Cat#Ant-bl-1
1,6-Hexanediol	Sigma-Aldrich	Cat#240117
2,5-Hexanediol	Sigma-Aldrich	Cat#H11904
2,2′-Thiodiethanol	Sigma-Aldrich	Cat#166782
DABCO 33-LV	Sigma-Aldrich	Cat#290734
VECTASHIELD Hard Set Mounting Medium with DAPI	Vector laboratories	Cat#H-1500
TRI Reagent	Molecular Research Center	Cat#TR118
cOmplete, EDTA free Protease Inhibitor Cocktail	Roche	5056489001
TransIT LT-1 Reagent	Mirus	Cat#MIR2300
Proteinase K	Roche	Cat#3115828001
Blocking reagent	Roche	Cat#11096176001
Glutaraldehyde (for EM)	Euromedex	Cat#16220
Formaldehyde (for EM)	Euromedex	Cat#19200
Critical Commercial Assays		
High Capacity cDNA Reverse Transcription Kit	Thermo Fisher Scientific	Cat#4368813
Stellaris FISH probe (Human NEAT1_5 with Quaser 570 Dye)	LGC Biosearch Technologies	Cat#SMF-2036-1

(*Continued on next page*)

Continued

REAGENT or RESOURCE	SOURCE	IDENTIFIER
Stellaris FISH probe (Human NEAT1_m with Quaser 570 Dye)	LGC Biosearch Technologies	Cat#SMF-2037-1
RPAIII Ribonuclease Protection Assay Kit	Thermo Fisher Scientific	Cat#AM1414
BRIC kit	MBL	Cat#RN1007
T7 Endonuclease I	NEB	Cat#M0302L
Dynabeads protein G	Thermo Fisher Scientific	Cat#10004D
Dynabeads His-Tag Isolation & Pulldown	Thermo Fisher Scientific	Cat#10103D
Anti-FLAG M2 magnetic beads	Sigma-Aldrich	Cat#M8823
Tamavidin2-REV Magnetic Beads	WAKO	Cat#136-18341
Biotin RNA labeling Mix	Sigma-Aldrich	Cat#11685597910
MEGAscript T7 Transcription Kit	Thermo Fisher Scientific	Cat#AM1333
MEGAscript SP6 Transcription Kit	Thermo Fisher Scientific	Cat#AM1330
Nick-translation	Roche	Cat#10976776001
Biotin-16-dUTP	Roche	Cat#11093070910
Deposited Data		
PAR-CLIP data	This paper	GSE113349
Raw image files	This study	Mendeley Data https://doi.org/10.17632/29k48yvp6b.2
TDP-43 iCLIP	Tollervey et al., 2011	SRA: ERX016992
FUS CLIP-seq	Zhou et al., 2013	GEO: GSE50178
Experimental Models: Cell Lines		
Human HAP1 cell line	Horizon Discovery	Cat#C631, RRID:CVCL_Y019
HAP1 mutant cell lines	This paper	See Table S1
HAP1 NONO knockout cell line	This paper	See Table S1
HAP1 FUS knockout cell line	Horizon Discovery	Cat#HZGHC001314c006
U-2 OS cell line	ATCC	Cat#ATCC HTB-96, RRID:CVCL_0042
Oligonucleotides		
Primers for qPCR	Sigma-Aldrich	See Table S2
Recombinant DNA		
Plasmid: pcDNA5/FRT/TO/i/FLAG/MCP/GFP-NLS	This paper	N/A
Plasmid: pcDNA5/FRT/TO/i/FLAG/MCP/NONO	This paper	N/A
Plasmid: pcDNA5/FRT/TO/i/FLAG/MCP/SFPQ	This paper	N/A
Plasmid: pcDNA5/FRT/TO/i/FLAG/MCP/FUS	This paper	N/A
Plasmid: pcDNA5/FRT/TO/i/FLAG/MCP/RBM14	This paper	N/A
Plasmid: pcDNA5/FRT/TO/i/FLAG/MCP/NONOΔNOPS	This paper	N/A
Plasmid: pcDNA5/FRT/TO/i/FLAG/MCP/NONOΔCC	This paper	N/A
Plasmid: pcDNA5/FRT/TO/i/FLAG/MCP/NONOΔPLD	This paper	N/A
Plasmid: PX330-U6-Chimeric_BB-CBh-hSpCas9 (PX330)	Addgene	Plasmid #42230
Plasmid: PX330-B/B	This paper	N/A
pcDNA6/TR	Thermo Fisher Scientific	Cat#V102520
Software and Algorithms		
Volocity 6.3	PerkinElmer	http://cellularimaging.perkinelmer.com/downloads
Prism 7	GraphPad Software	https://www.graphpad.com
ImageJ, Fiji, version 1.0	Open source image processing software	https://fiji.sc/
Zen	ZEISS	N/A
Metamorph	Molecular Devices	N/A

CONTACT FOR REAGENT AND RESOURCE SHARING

Further information and requests for resources and reagents should be directed to and will be fulfilled by the Lead Contact, Tetsuro Hirose (hirose@igm.hokudai.ac.jp).

EXPERIMENTAL MODEL AND SUBJECT DETAILS

HAP1 cell line

HAP1 cells were maintained in IMDM (GIBCO) supplemented with 10% FBS (GIBCO) and Penicillin-Streptomycin (Nacalai Tesque). HAP1 mutant cell lines established in this study are listed in Table S1. HeLa cells and U-2 OS cells were maintained in DMEM containing high glucose and pyruvate (GIBCO) supplemented with 10% FBS (Serana) and Penicillin-Streptomycin (GIBCO).

METHOD DETAILS

Plasmids

To express Cas9 and two sgRNAs from one vector, the PX330 vector bearing an additional U6-driven sgRNA expression cassette (PX330-B/B) was constructed by inserting a second sgRNA expression cassette containing a BsaI sgRNA cloning site that was amplified from the PX330 vector bearing a BsaI sgRNA cloning site instead of the original BbsI site by primers (Forward: TCTAGA GAGGGCCTATTTCCCATGAT, Reverse: TCTAGAGCCATTTGTCTGCAGAATTG) into the XbaI site of the PX330 plasmid (Addgene). pcDNA5/FRT/TO/i/FLAG vector was generated by inserting the Ftz intron into the AflII site of pcDNA5/FRT/TO/FLAG used previously (Yamazaki et al., 2012). To construct MCP fusion protein expression vector (pcDNA5/FRT/TO/i/FLAG/MCP), the MCP gene was inserted into the KpnI site of pcDNA5/FRT/TO/i/FLAG. To generate FLAG-MCP-GFP-NLS, FLAG-MCP-NONO, FLAG-MCP-SFPQ, FLAG-MCP-FUS, and FLAG-MCP-RBM14 expression vectors, the MCP-GFP-NLS was inserted into the KpnI site of pcDNA5/FRT/TO/i/FLAG, the NONO ORF was inserted using the BamHI and XhoI sites of pcDNA5/FRT/TO/i/FLAG/MCP, and the SFPQ, FUS, or RBM14 ORF was inserted into the EcoRV site in pcDNA5/FRT/TO/i/FLAG/MCP. To construct plasmids expressing FLAG-MCP-NONO mutants including NONOΔNOPS (Δ219–272aa), NONOΔCC (1–312aa fused with SV40 NLS), and NONOΔPLD (Δ1–52aa), the deletions were introduced by a conventional cloning or site-directed mutagenesis approach. To construct the knock-in vector for 6 × MS2BS, knock-in sgRNA targeting sites (GCATCGTACGCGTACGTGTT) were inserted into both sides of the 6 × MS2BS by PCR amplification and the PCR fragments were sub-cloned into the pCR-Blunt II-TOPO vector (Thermo Fisher Scientific).

Genome editing using CRISPR/Cas9

PX330 or PX330-B/B was used for genome editing of the HAP1 cells. sgRNAs targeting NEAT1 were designed using the CRISPR Design website (crispr.mit.edu) (Table S1). Using PX330-B/B, two sgRNAs were cloned into BbsI and BsaI/Eco31I sites according to the methods described previously (Ran et al., 2013). To delete the portions of NEAT1, the PX330-B/B plasmids (2 μg) containing two sgRNA sequences were co-transfected with pcDNA6/TR plasmids (0.2 μg) containing the blasticidin resistance gene (Thermo Fisher Scientific) into HAP1 cells (1.5 × 10^6 cells) by Nucleofector Kit V (Lonza) with a Nucleofector device (Lonza) using program "X-005" according to the manufacturer's instructions. For knock-in of the 6 × MS2 site into the NEAT1 locus, three kinds of plasmids including 1) PX330-B/B (2 μg) expressing two sgRNAs (a knock-in sgRNA to cut both sides of 6 × MS2BS on the knock-in vector to facilitate genomic integration: GCATCGTACGCGTACGTGTT, and a sgRNA targeting the NEAT1 locus: TACCGCATATCTGTGT ACAT), 2) a knock-in vector for 6 × MS2BS (2 μg), and 3) pcDNA6/TR plasmids (0.2 μg) were transfected, similarly using a Nucleofector device (Lonza). To establish NONO knockout HAP1 cells, the sgRNA (see Table S1) was selected from GeCKO v2 libraries (Sanjana et al., 2014) and cloned into the BbsI site of PX330 (Addgene). The plasmids (2 μg) and pcDNA6/TR plasmids (0.2 μg) were transfected similarly using a Nucleofector device (Lonza). To enrich the plasmid-transfected cells, the HAP1 cells were treated with 20 μg/ml blasticidin (InvivoGen) for 3 days, starting 1 day after transfection. Subsequently, the cells were diluted into 96-well plates for selection of single clones. The selected clones were lysed by proteinase K treatment (200 μg/ml proteinase K [Roche], 20 mM Tris-HCl pH 8.0, 5 mM EDTA, 400 mM NaCl, and 0.3% SDS at 55°C for 1 h, followed by proteinase K inactivation; 95°C for 15 min). Then, the lysates were subjected to PCR analysis to amplify the genomic regions flanking the guide RNA target sites for detecting deletions or insertions using KOD FX Neo enzyme (TOYOBO). To detect small deletions in the NONO knockout cell lines, a T7 endonuclease I (NEB) cleavage assay was performed on the amplified PCR products. The indel-positive clones were further confirmed by sequencing. Finally, the absence of protein expression was confirmed by immunoblotting.

Plasmid transfection

For MS2 tethering and immunoprecipitation (IP) experiments, HAP1 cells (1.8 × 10^5 cells/well) were cultured on coverslips (ZEISS) in a 6-well plate overnight and plasmids (1.5 μg) were transfected using 5 μL of TransIT LT-1 (Mirus). The cells were cultured for 48 h, including 6 h of MG132 treatment. Then, the cells were subjected to each experiment.

RNA-FISH and immunofluorescence

RNA-FISH and immunofluorescence were performed as previously described (Kawaguchi et al., 2015; West et al., 2016). The RNA probes were synthesized using T7 or SP6 RNA polymerase and a digoxigenin (DIG) or a fluorescein (FITC) RNA labeling kit (Roche). Linearized plasmids (1 μg) containing a NEAT1 fragment (see Table S2 for details) were used as templates. For confocal microscopic analyses, the cells were grown on coverslips (Matsunami; micro cover glass; 18 mm round; thickness, 0.16–0.19 mm) and fixed with 4% paraformaldehyde/PBS at room temperature for 10 min. Then, the cells were washed with 1 × PBS, permeabilized with 0.5% Triton X-100/PBS for 5 min, and washed three times with 1 × PBS. Subsequently, the cells were dipped in 100% ethanol for 5 min and then dried. Dehydrated coverslips were incubated with pre-hybridization solution (50% formamide, 1 × Denhardt's salt [Sigma-Aldrich], 2 × SSC, 100 mM EDTA, 100 μg/ml yeast tRNA, and 0.01% Tween 20) at 55°C for 1 h and then incubated with hybridization solution (50% formamide, 1 × Denhardt's salt [Sigma-Aldrich], 2 × SSC, 100 mM EDTA, 100 μg/ml yeast tRNA, 0.01% Tween 20, and 5% Dextransulfate [Sigma-Aldrich]) containing DIG- or FITC-labeled RNA probes (final concentration: 100 ng/coverslip) at 55°C overnight. After hybridization, the coverslips were washed twice with prewarmed wash buffer (50% formamide, 2 × SSC, and 0.1% Tween 20) at 55°C for 15 min. Then, excess RNA probes were digested with 10 μg/ml RNase A (Nacalai Tesque) in NTET buffer (10 mM Tris-HCl [pH 8.0], 1 mM EDTA, 500 mM NaCl, and 0.1% Tween 20) at 37°C for 30 min. The coverslips were washed with buffer (2 × SSC and 0.01% Tween 20) at 55°C for 15 min and washed twice with a second buffer (0.1 × SSC and 0.01% Tween 20) at 55°C for 15 min. The coverslips were subsequently washed with TBST (1 × TBS containing 0.1% Tween 20) and incubated with 1 × blocking solution (Blocking reagent [Roche] and TBST) for blocking at room temperature for 1 h. Then, the coverslips were incubated with primary antibodies in 1 × blocking solution at room temperature for 1 h, washed three times with TBST for 5 min, incubated with secondary antibodies in 1 × blocking solution at room temperature for 30 min, and washed three times with TBST for 5 min. The coverslips were mounted with VECTASHIELD Hard Set Mounting Medium with DAPI (Vector). Confocal images were acquired using a confocal laser scanning microscope FV1000D (Olympus).

For super-resolution microscopic analyses using Structured Illumination Microscopy (SIM), the cells were grown on coverslips (ZEISS; Cat#0109030091; 18 × 18 mm; thickness no. 1.5H, 170 ± 5 μm) and fixed with 4% paraformaldehyde/PBS at 4°C overnight. The coverslips were subsequently washed with 1 × PBS and then Milli-Q water. Then, the coverslips were treated with 0.2 N HCl at room temperature for 20 min and washed with Milli-Q water. The coverslips were incubated in Proteinase K buffer (10 mM Tris-HCl [pH 8.0] and 10 mM EDTA [pH 8.0]), then an equal volume of 2 × Proteinase K solution (3.3 μg/ml Proteinase K [Roche], 10 mM Tris-HCl [pH 8.0], and 10 mM EDTA [pH 8.0]) was added and the coverslips were incubated at 37°C for 7 min. To stop the Proteinase K reaction, the coverslips were treated with 0.2% glycine/PBS at room temperature for 10 min. Then, the coverslips were washed with 1 × PBS and fixed again with 4% paraformaldehyde/PBS at room temperature for 10 min. The coverslips were washed twice with 1 × PBS, once with Milli-Q water, and once with 100% ethanol for 5 min, and air-dried. Rehydrated coverslips were pre-hybridized with pre-hybridization solution at 55°C for 1 h and then incubated with hybridization solution containing DIG- or FITC-labeled RNA probes (final concentration: 500 ng/coverslip) at 55°C overnight. After hybridization, the coverslips were proceeded to the washing, blocking, and immunofluorescence steps of the conventional method described above. After the incubation with secondary antibodies, the coverslips were washed with TBST and 1 × PBS, and then fixed again with 4% paraformaldehyde/PBS at room temperature for 10 min. Then, the coverslips were washed once with PBS and twice with TBST. The coverslips were mounted with 97% TDE (Sigma-Aldrich) containing DABCO 33-LV (Sigma-Aldrich) as an anti-fade reagent. SIM images were captured using ELYRA PS.1 (ZEISS) with 100 × objective lens as previously described (West et al., 2016).

For the treatment with 1,6-Hexanediol or 2,5-Hexanediol, 1,6-Hexanediol or 2,5-Hexanediol dissolved in the HAP1 culture medium was added to cells at room temperature for 5 min. After these treatments, the cells were fixed with 4% paraformaldehyde/PBS followed by the RNA-FISH and immunofluorescence procedure described above. The antibodies used in the RNA-FISH and immunofluorescence are listed in the Key Resources Table. NEAT1 FISH probes against 5′ (+1 to +1000), middle (+12786 to +13811), 15.4–16.6k (+15401 to +16612), and 3′ regions (+21743 to +22580) were transcribed as antisense RNAs.

Single-molecule FISH (smFISH)

Stellaris FISH probes to the NEAT1 5′ region (LGC Biosearch Technologies) and NEAT1 middle region (LGC Biosearch Technologies) were used for single molecule FISH (smFISH). The smFISH was performed according to the manufacturer's instructions. The cells were cultured on coverslips (18 mm round) and then fixed with 4% paraformaldehyde/PBS at room temperature for 10 min. Then, the fixed cells were washed twice with 1 × PBS and immersed in 70% ethanol for at least 1 h at 4°C for permeabilization. After removing the 70% ethanol, wash buffer (2 × SSC and 10% formamide) was added and the coverslips were incubated for 5 min. Then, the 50 μL hybridization solutions (2 × SSC, 100 mg/ml dextran sulfate, and 10% formamide) containing Stellaris NEAT1 probes (final concentration: 125 nM) were dropped onto the coverslips in the humidified chamber, and were incubated for 16 h in the dark. The coverslips were washed with wash buffer at 37°C for 30 min and with 2 × SSC at room temperature for 5 min. The coverslips were mounted with VECTASHIELD Hard Set Mounting Medium with DAPI (Vector).

Reverse transcription-quantitative PCR (RT-qPCR)

Total RNAs were purified with TRI reagent (Molecular Research Center) as previously described (Chujo et al., 2017). Briefly, homogenates of cells with TRI reagent were heated at 55°C for 20 min with 1000 rpm agitation. Total RNAs were purified according to the manufacturer's instructions. To quantify NEAT1_2 levels, the total RNAs (1 μg) were reverse-transcribed by High Capacity cDNA

Reverse Transcription Kit (Thermo Fisher Scientific) with random hexamer primers. To quantify NEAT1_1 specifically, cDNA was reverse-transcribed using dT_{20} primers. Aliquots of cDNA were amplified by qPCR using LightCycler 480 SYBR Green I Master reagent (Roche) according to the manufacturer's instructions (see Table S2 for primer sets).

RNase protection assay (RPA)

RNase protection assays (RPAs) were performed using RPAIII kit (Thermo Fisher Scientific). Total RNAs were purified from the HAP1 cell lines using TRI reagents according to the manufacturer's instructions with a modification of heat treatment at 55°C for 20 min with 1000 rpm agitation. The total RNA (5 μg) was hybridized with ^{32}P-labeled antisense probes (NEAT1_1 and NEAT1_2 boundary region, and U12) synthesized using T7 RNA polymerase (Takara) (Naganuma et al., 2012). RNase A/T1 digestion was performed to eliminate unhybridized single-stranded RNA probes. The protected RNA fragments were separated on 6% PAGE gels containing 7 M urea. Radioactive RNA bands were visualized and quantified with an FLA-7000 analyzer (Fuji).

5-bromouridine pulse-chase analysis

The 5-bromouridine pulse-chase analyses were performed using BRIC kit (MBL) according to the manufacturer's instructions. The HAP1 cells were seeded at 1 million cells per 10 cm dish and cultured overnight. Then, BrU solution was added and cultured for BrU-labeling for 24 h. The cells were washed three times with 1 × PBS, and then fresh culture medium was added. Samples were collected at several time points. The total RNAs from the samples were purified using TRI reagent (MRC) as described above. The purified BrU-labeled RNAs were immunoprecipitated with anti-BrdU monoclonal antibody immobilized on protein G magnetic beads. The immunoprecipitated RNAs were subjected to reverse transcription-quantitative PCR (RT-qPCR) analyses using GAPDH as a loading control.

Immunoblotting

Cells were lysed in immunoprecipitation (IP) lysis buffer (50 mM Tris-HCl pH 8.0, 150 mM NaCl, 1% Triton X-100, and complete EDTA-free protease inhibitor cocktail [Roche]) and then disrupted by five pulses of sonication for 5 s. The cell lysates were cleared by centrifugation, and the protein concentration was determined using the Bradford method. After adding SDS sample buffer, the samples were heated at 95°C for 5 min and separated by SDS-PAGE. After electrophoresis, the proteins were transferred to FluoroTrans W membrane (PALL) by electroblotting. The antibodies used are listed in the Key Resources Table.

Electron microscopy

Ultrastructural studies were carried out on ultra-thin sections of Lowicryl K4M-embedded cell pellets as previously described (Souquere and Pierron, 2015). Duplicated samples of WT and mutant HAP1 cells grown in the absence or presence of 5 μM MG132 were fixed *in situ* with 1.6% glutaraldehyde (Electron Microscopic Sciences) or 4% formaldehyde (Electron Microscopic Sciences), scraped off from plastic containers, and centrifuged. Cell pellets were equilibrated in 30% methanol and deposited in a Leica EM AFS2/FSP automatic reagent handling apparatus (Leica Microsystems). Lowicryl polymerization under UV was performed for 40 h at −20°C and 40 h at +20°C.

For immunogold electron microscopy (I-EM), ultra-thin sections were incubated at room temperature for 1 h with the primary antibody (mouse anti-NONO [BD Biosciences, 1/20 dilution in PBS] or rabbit anti-BRG1 [Bethyl Laboratories, 1/25 dilution in PBS]) and for 30 min with the secondary anti-mouse IgG or anti-rabbit IgG antibody coupled to 10 nm gold particles (BBInternational). Thin sections were briefly contrasted with uranyl acetate and analyzed with a Tecnai Spirit (FEI). Digital images were taken with a SIS MegaviewIII charge-coupled device camera (Olympus). Short axes (Sx), long axes (Lx), and surface areas of nuclear body sections were determined with AnalySIS (Olympus Soft Imaging Solutions).

For high resolution *in situ* hybridization (EM-ISH), ultra-thin sections of formaldehyde-fixed cells were occasionally pre-treated with protease (0.2 mg/ml) for 15 min at 37°C to enhance access of the biotinylated DNA probes to the NEAT1 targets. Hybridization conditions and detection of RNA/DNA hybrids with goat anti-biotin antibody conjugated to 10 nm gold particles (BBI International) were as previously described (Souquere et al., 2010; Souquere and Pierron, 2015).

DNA probes were PCR-amplified DNA fragments biotinylated by nick translation (Roche) with biotin-16-dUTP (Roche) instead of TTP in the reaction mix. The NEAT1_5′ DNA probe (+230–1721 and +1751–3244) and D2 probe (+12841–14160 and +14735–15897) were as previously described (Souquere et al., 2010). The NEAT1 5′ end probe (+1 to +1000) was nick-translated for 40 min at 15°C and following denaturation hybridized at 60°C for 120 min.

PAR-CLIP and mapping of CLIP-seq data

PAR-CLIP experiments were performed based on the method of Hafner et al. (Hafner et al., 2010). Cells cultured in normal growth media were supplemented with 4SU for 14 h. Cells were washed with PBS and then irradiated with 365 nm UV at 0.15 J/cm^2 in a Stratalinker 2400. Cells were harvested, lysed in NP-40 lysis buffer, and passed through a 32-gauge needle. Lysates were cleared by centrifugation and then incubated with RNase T1 (Fermentas). Lysates were precleared using Protein G Dynabeads (Invitrogen), after which RNA-protein complexes containing NONO were immunoprecipitated with NONO antibody (Souquere et al., 2010) conjugated to Protein G Dynabeads (Thermo Fisher Scientific). Following IP, beads were washed and then resuspended in dephosphorylation buffer and Calf intestinal alkaline phosphatase (New England Biolabs). Beads were then washed and incubated in

polynucleotide kinase buffer, and RNA was radiolabeled with γ-^{32}P-ATP (Perkin Elmer). Radiolabeled protein-RNA complexes were removed from Dynabeads, then resolved by SDS-PAGE on a NuPAGE Novex 4%–12% Bis-Tris Protein Gel (Thermo Fisher Scientific). Using ^{32}P radiography, RNA-protein complexes were excised from the gel, and electroeluted in D-Tube Dialyzer midi tubes (Merck Millipore). Electroeluant was digested with Proteinase K (Fermentas), and RNA was then extracted from samples using miRNAeasy Micro Kit (QIAGEN). RNA extracted from PAR-CLIP was converted into a cDNA library using TruSeq small RNA Kit v2 (Illumina) with a size selection range of 145–327 bp (RNA of 18–200 nt) and Illumina sequencing with 50 bp single reads.

Cutadapt (http://code.google.com/p/cutadapt) was used to remove the sequencing adapters, and unique reads were aligned to the human reference genome (hg38) using Bowtie (http://bowtie-bio.sourceforge.net) allowing up to one mismatch (-v 1 -m 1). FUS HITS-CLIP and TDP-43 iCLIP data were used by reanalyzing deposited datasets (see Key Resources Table).

Immunoprecipitation

HAP1 cells (m13–16.6k/6 × MS2BS) transfected with the indicated plasmids using TransIT LT-1 reagent (Mirus) were cultured for 48 h including the last 6 h with MG132 treatment, washed with cold PBS, and harvested by cell scrapers. The collected cells were lysed in the IP lysis buffer (50 mM Tris-HCl pH 8.0, 150 mM NaCl, 1% Triton X-100, and complete EDTA-free protease inhibitor cocktail [Roche]) by three pulses of sonication for 5 s. The cell lysates were cleared by centrifugation, and the protein concentration was determined using the Bradford method. The lysates were diluted with IP lysis buffer (protein concentration: ~2 mg/ml) and treated with RNase A (1 μg/ml) at 4°C for 1 h. Then, the lysates were mixed with anti-FLAG M2 magnetic beads (Sigma-Aldrich) and rotated at 4°C overnight. The beads were washed five times with IP lysis buffer. The IP samples were recovered by adding SDS sample buffer.

For immunoprecipitation of NONO from HeLa nuclear extract (NE), 25 μL of HeLa NE (CILBIOTECH) spun at 20,000 × *g* for 5 min were mixed with 100 μL of IP buffer (1 × PBS, 0.1% Triton X-100, 0.6 mM PMSF, and complete EDTA-free protease inhibitor cocktail [Roche]) and 1 μL RNase A (Nacalai Tesque, 10 mg/ml). Control antibodies (Santa Cruz, normal mouse IgG_1, 3.75 μg) were conjugated with 15 μL of Dynabeads Protein G Magnetic Beads (Thermo Fisher Scientific) by rotating the tubes at room temperature for 1 hour. The beads were washed with IP buffer to wash out unbound antibodies. Then the antibody-conjugated beads were mixed with the NE solution prepared above and rotated at 4°C for 1.5 hours to preclear the NE solution. For IP, control (Santa Cruz, normal mouse IgG_1) and anti-NONO mouse monoclonal antibodies (3.75 μg) (BD Biosciences) were conjugated with 15 μL of Dynabeads Protein G Magnetic Beads (Thermo Fisher Scientific) by rotating the tubes at room temperature for 1 hour. The beads were washed with IP buffer to wash out unbound antibodies. Then the antibody-conjugated beads were mixed with the precleared NE solution and rotated at 4°C for overnight. The beads were washed 5 times with different washing buffers shown below: normal wash buffer (1 × PBS, 0.1% Triton X-100, and 0.6 mM PMSF), 1,6-hexanediol wash buffer (normal wash buffer containing 10% of 1,6-hexanediol), 2,5-hexanediol wash buffer (normal wash buffer containing 10% of 1,6-hexanediol), or high salt (HS) wash buffer (normal wash buffer containing 1 M NaCl). For elution, to minimize the elution of IgG from the beads, SDS sample buffer without DTT was added to the washed beads and the beads were kept at room temperature for 20 minutes with agitation using an Eppendorf ThermoMixer (1000 rpm). Then the eluates were recovered and DTT (5 mM) was added. The eluates were boiled and subjected to SDS-PAGE, followed by Coomassie blue staining or immunoblotting.

RNA pull-down

Biotinylated RNAs were synthesized with T7 or SP6 RNA polymerase (Roche) and Biotin RNA labeling Mix (Roche), template DNAs were degraded by DNase I (Thermo Fisher Scientific) treatment, and the biotinylated RNAs were purified by gel filtration column (CENTRI SEP Spin Column; PRINCETON SEPARATIONS). HeLa NE was prepared as previously described (Lee and Green, 1990) or purchased from CILBIOTECH. The NE (50 μl) spun at 20,000 × *g* for 5 min was mixed with 150 μL of RNA pulldown buffer (1 × PBS, 0.1% Triton X-100, 0.6 mM PMSF, and complete EDTA-free protease inhibitor cocktail [Roche]) (final protein concentration was approximately 2 mg/ml). The NE (200 μl) was precleared by mixing 20 μL Tamavidin2-REV Magnetic Beads (WAKO) washed with RNA pulldown buffer and then rotating at 4°C for 1 h. *In vitro* transcribed RNAs (1 μg in 10 mL UltraPure Distilled Water [Thermo Scientific]) were heated at 90°C for 2 min and then cooled on ice for 2 min. An equal volume (10 μl) of 2 × RNA structure buffer (20 mM Tris-HCl pH 7.4, 0.2 M KCl, and 20 mM $MgCl_2$) was added and kept at room temperature for 20 min to allow proper secondary structure formation. The folded RNAs were mixed with washed Tamavidin2-REV Magnetic Beads (20 μl) and rotated at 4°C for 1 h. The unbound RNAs were washed with cold RNA pulldown buffer, and then the RNA-bound Tamavidin2-REV Magnetic Beads (20 μl) were mixed with the precleared NE (200 μl). They were rotated at 4°C for 3 h and washed five times with cold wash buffer (1 × PBS, 0.1% Triton X-100, and 0.6 mM PMSF), and then the bound proteins were eluted at 95°C for 5 min in SDS sample buffer. The eluates were subjected to SDS-PAGE, followed by Coomassie blue staining or immunoblotting.

Bead aggregation assay

The same procedure described in the RNA pulldown method was performed until washing except for the use of washing buffer containing 10% 1,6-HD or 2,5-HD in the indicated samples. To visualize RNAs on beads, Fluorescein-Avidin DN (VectorLab, 1: 500 dilution) was added to the mixtures of the RNA bound beads and NE solutions. After the washing, 20 μL of the beads suspended in the washing buffer was dropped onto a bottom-glass 8-well chamber and observed by EVOS FL AUTO imaging system (Thermo Fisher Scientific). The obtained images were analyzed using the function "Analyze Particles" with Fiji (NIH).

Affinity depletion from NE

Depletion of NONO/SFPQ from NE was performed using Ni-NTA beads to capture NONO through its N-terminal histidine rich sequence (Snijders et al., 2015). 100 μL of Dynabeads His-Tag Isolation and pulldown beads (Thermo Fisher Scientific) or 100 μL of Dynabeads M-280 Sheep anti-mouse IgG (Thermo Fisher Scientific) as a mock depletion were mixed with 250 μL of NE (CILBIOTECH) containing 0.1% Triton X-100, 0.6 mM PMSF, and 10 mM Immidazole. After 1 hour rotation at 4°C, the recovered NE was subjected to a second depletion step as described above. After the second depletion, the recovered NEs were subjected to the bead aggregation assay and SDS-PAGE, followed by Coomassie blue staining or immunoblotting.

QUANTIFICATION AND STATISTICAL ANALYSIS

Volocity software (PerkinElmer) was used for quantification of the paraspeckle number, intensity, and size of smFISH signals with an intensity threshold. Fiji software (NIH) was used for line profiles and bead aggregation assay. Prism7 software (GraphPad) was used for the statistical analyses. Kruskal-Wallis test with Dunn's multiple comparison test was used for Figures 3C, 3E, 5C, 7H, S3D, S3F, and S5D. Mann-Whitney test (two-tailed) was used for Figures 4H, 7E, and S6H. Fisher's exact test (two-sided) was used for Figures 5E and 5G.

DATA AND SOFTWARE AVAILABILITY

The accession number for the PAR-CLIP reported in this paper is GEO: GSE113349. Raw image files were deposited on Mendeley Data: https://doi.org/10.17632/29k48yvp6b.2.